# Excessive rDNA Transcription Drives the Disruption in Nuclear Homeostasis during Entry into Senescence in Budding Yeast

Sandrine Morlot, Jia Song, Isabelle Léger-Silvestre, Audrey Matifas, Olivier Gadal, Gilles Charvin

▶ **To cite this version:**

Sandrine Morlot, Jia Song, Isabelle Léger-Silvestre, Audrey Matifas, Olivier Gadal, et al.. Excessive rDNA Transcription Drives the Disruption in Nuclear Homeostasis during Entry into Senescence in Budding Yeast. Cell Reports, 2019, 28 (2), pp.408-422.e4. 10.1016/j.celrep.2019.06.032 . hal-03096871

**HAL Id: hal-03096871**
**https://hal.science/hal-03096871**

Submitted on 7 Jan 2021

**HAL** is a multi-disciplinary open access archive for the deposit and dissemination of scientific research documents, whether they are published or not. The documents may come from teaching and research institutions in France or abroad, or from public or private research centers.

L'archive ouverte pluridisciplinaire **HAL**, est destinée au dépôt et à la diffusion de documents scientifiques de niveau recherche, publiés ou non, émanant des établissements d'enseignement et de recherche français ou étrangers, des laboratoires publics ou privés.

Article

Cell Reports

# Excessive rDNA Transcription Drives the Disruption in Nuclear Homeostasis during Entry into Senescence in Budding Yeast

## Graphical Abstract

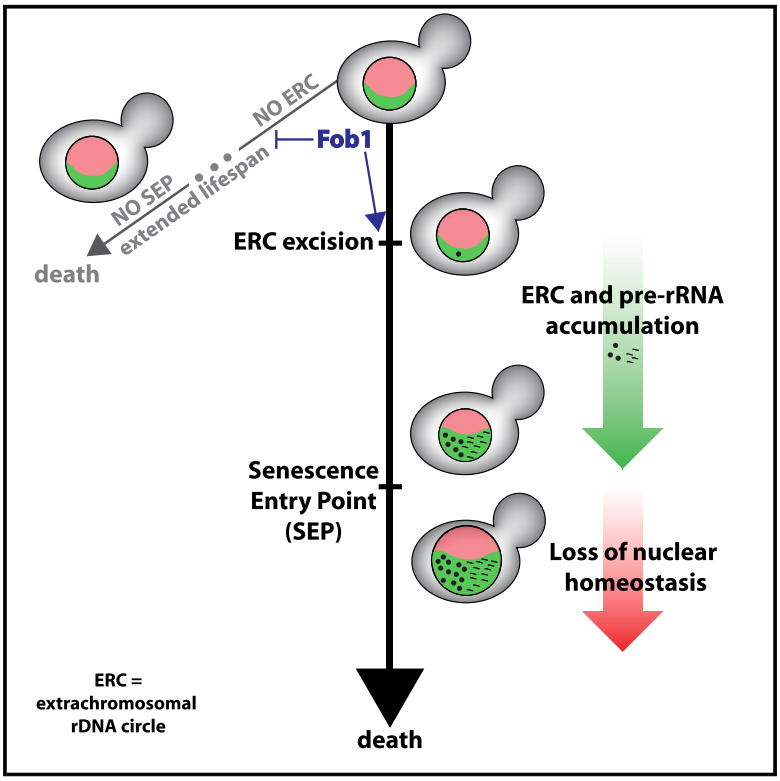


## Highlights

- Single-cell monitoring shows that ERC accumulation starts well before senescence
- ERC accumulation drives a large upregulation in pre-rRNA, but not ribosome, synthesis
- A strong loss of nuclear homeostasis occurs downstream of nucleolar defects
- Rejuvenation of daughters is ensured by asymmetrical nuclear partitioning

## Authors

Sandrine Morlot, Jia Song, Isabelle Léger-Silvestre, Audrey Matifas, Olivier Gadal, Gilles Charvin

## Correspondence

morlot@igbmc.fr (S.M.), charvin@igbmc.fr (G.C.)

## In Brief

The accumulation of extrachromosomal rDNA circles (ERCs) is a hallmark of aging in budding yeast. Morlot et al. show that ERCs accumulate ahead of senescence onset and fuel an excessive rDNA transcription, ultimately leading to impaired nuclear homeostasis and an irreversible cell cycle slowdown.

Morlot et al., 2019, Cell Reports *28*, 408–422
July 9, 2019 © 2019 The Authors.
https://doi.org/10.1016/j.celrep.2019.06.032

CellPress

OPEN ACCESS
CellPress

Cell Reports
Article

# Excessive rDNA Transcription Drives the Disruption in Nuclear Homeostasis during Entry into Senescence in Budding Yeast

Sandrine Morlot,[1,2,3,4,*] Jia Song,[1,2,3,4] Isabelle Léger-Silvestre,[5] Audrey Matifas,[1,2,3,4] Olivier Gadal,[5] and Gilles Charvin[1,2,3,4,6,*]

[1]Developmental Biology and Stem Cells Department, Institut de Génétique et de Biologie Moléculaire et Cellulaire, Illkirch 67400, France
[2]Centre National de la Recherche Scientifique, UMR7104, Illkirch 67400, France
[3]Institut National de la Santé et de la Recherche Médicale, U1258, Illkirch 67400, France
[4]Université de Strasbourg, Illkirch 67400, France
[5]Laboratoire de Biologie Moléculaire Eucaryote, Centre de Biologie Intégrative (CBI), Université de Toulouse, CNRS, UPS, Toulouse 31000, France
[6]Lead Contact
*Correspondence: morlot@igbmc.fr (S.M.), charvin@igbmc.fr (G.C.)
https://doi.org/10.1016/j.celrep.2019.06.032

## SUMMARY

**Budding yeast cells undergo a limited number of divisions before they enter senescence and die. Despite recent mechanistic advances, whether and how molecular events are temporally and causally linked during the transition to senescence remain elusive. Here, using real-time observation of the accumulation of extrachromosomal rDNA circles (ERCs) in single cells, we provide evidence that ERCs build up rapidly with exponential kinetics well before any physiological decline. We then show that ERCs fuel a massive increase in ribosomal RNA (rRNA) levels in the nucleolus, which do not mature into functional ribosomes. This breakdown in nucleolar coordination is followed by a loss of nuclear homeostasis, thus defining a chronology of causally related events leading to cell death. A computational analysis supports a model in which a series of age-independent processes lead to an age-dependent increase in cell mortality, hence explaining the emergence of aging in budding yeast.**

## INTRODUCTION

Budding yeast cells undergo a limited number of asymmetrical divisions before entering senescence and dying, a phenomenon known as replicative aging (Mortimer and Johnston, 1959). Although the replicative age of mother cells increases at each division, the newborn daughter cells are "rejuvenated," meaning that they have full replicative potential (Kennedy et al., 1994). To explain this phenomenon, it has long been proposed that aging cells accumulate detrimental factors that are lethal to the mother but are not inherited by daughter cells (Egilmez and Jazwinski, 1989). Since that hypothesis was first proposed, a large body of literature has established that yeast cell aging is accompanied by breakdown of many cellular functions, resulting in the loss of proteostasis (Erjavec et al., 2007), sterility (Smeal et al., 1996), genomic instability (McMurray and Gottschling, 2003), impairment in mitochondrial function (Veatch et al., 2009), cell cycle dysregulation (Neurohr et al., 2018), and nucleolar enlargement and fragmentation (Sinclair et al., 1997), among other defects.

Based on these observations, a consensus has emerged in which cellular aging is viewed as a progressive phenomenon involving gradual deterioration of physiological functions, leading to cell death. In contrast to this classical view, which is largely based on observations of cells in bulk culture, longitudinal tracking of individual cells from birth to death revealed the existence of a well-defined time point in cellular lifespan beyond which the cell cycle duration rapidly increases before cell death, which is a time point previously referred to as the senescence entry point (SEP) (Fehrmann et al., 2013). The origin of the discrepancy between single-cell versus population measurements originates from cell-cell variability in the time of death. Indeed, even if the appearance of a given hallmark of age is abrupt during cellular lifespan, it was shown that pooling of data from individual cells with heterogeneous lifespans considerably attenuate the average dynamics of this marker (Figure S1A) (Fehrmann et al., 2013). Hence, bulk measurements do not faithfully capture the true kinetics of aging markers during the entry into senescence, and this may lead to misleading interpretations. Similarly, an analysis of bulk populations of cells with heterogeneous lifespans would limit our ability to temporally order the onset of aging marks, thus precluding the identification of their causal relationships (Figure S1B). This explains in part why, despite numerous correlations between age and accumulation of diverse factors (for example, protein aggregates [Erjavec et al., 2007], mitochondrial defects [Veatch et al., 2009], and genomic instability [McMurray and Gottschling, 2003]) in *Saccharomyces cerevisiae* and other model organisms, a clear and causal chain of events explaining entry into senescence remains to be unraveled.

In yeast, one factor proposed to regulate aging is the accumulation of extrachromosomal rDNA circles (ERCs) within mother cells (Sinclair and Guarente, 1997) that are asymmetrically apportioned and retained in the mother upon cell division

 © 2019 The Authors.
This is an open access article under the CC BY-NC-ND license (http://creativecommons.org/licenses/by-nc-nd/4.0/).

(Denoth Lippuner et al., 2014b; Shcheprova et al., 2008). ERCs are self-replicating sequences formed by the excision of repeats from the rDNA cluster, a genomic region located on chromosome XII that contains about 150–200 repeats of rRNA genes. Formation of ERCs is favored by these repeated sequences and by the presence of a replication fork barrier mediated by Fob1, which prevents collision between the DNA replication and rDNA transcription machineries, thereby favoring double-strand breaks and recombination events (Brewer and Fangman, 1988; Kobayashi, 2003). However, it is not yet known whether and how ERC accumulation is detrimental to cells (Ganley et al., 2009) or whether ERC excision, a potentially stochastic event, is temporally and mechanistically related to the onset of cell cycle slowdown (SEP) observed in aging mothers.

To address these questions, we monitored the replicative lifespan (RLS) of individual yeast cells by using a microfluidics-based imaging system (Goulev et al., 2017). We quantitatively analyzed the sequence of events driving both the entry into senescence in mother and the rejuvenation in daughter cells. Importantly, our experimental data support a model in which a series of age-independent processes lead to an age-dependent increase in cell mortality, hence explaining the emergence of aging in a simple unicellular organism.

## RESULTS

### ERCs Accumulate Exponentially before Entry into Senescence

To test the hypothesis that ERCs may be involved in driving the abrupt onset of SEP in aging mother cells, we measured the total number of rRNA gene copies (i.e., chromosomal and ERC rRNA gene repeats) in single yeast cells over their entire lifespans. To this end, we used a previously described microfluidics device in which individual mother cells are trapped in cavities and imaged at the single-cell level from birth to death (Goulev et al., 2017). To track rDNA copy number, we used a strain in which 50 repeats of the LacO sequence are inserted into each repeat of the nucleolar rRNA gene cluster (Miyazaki and Kobayashi, 2011). Thus, by co-expressing a GFP-LacI fusion protein and the nucleolar marker Net1-mCherry, the total size of the rDNA loci can be quantified (Figure 1A). Fluorescence imaging of these cells showed the presence of nucleolar-localized GFP throughout the cell lifespan, as expected (Figure 1B; Video S1), with a marked increase in GFP toward the end of the lifespan that was concomitant with the SEP (Figure 1C). We calculated the time of onset of SEP for each trajectory based on piecewise linear fitting to the dynamics of the individual cell cycle durations (as previously reported [Fehrmann et al., 2013] see also STAR Methods and Figure S2), which enabled alignment of the nucleolar GFP-LacI fluorescence signal and confirmed the marked accumulation of rDNA copies preceding the SEP (Figure 1D). This analysis revealed an almost 10-fold increase in the number of rRNA gene copies in post-SEP compared with pre-SEP cells (Figure 1E), which was paralleled by a large increase in total Net1-mCherry fluorescence (Figures S3A and S3B).

By further quantifying the dynamics of the average GFP-LacI fluorescence signal over time, we found an excellent agreement to an exponential fit with a doubling time $\tau$ of 1.6 ± 0.5 generations, providing direct evidence that a rapid multiplicative process governs the accumulation of the rDNA copy number (see Figure 1E and STAR Methods for details). Instead, when we analyzed average data after alignment of single-cell trajectories from birth (Figures S3E and S3F) or death (Figures S3G and S3H), rather than at the SEP, we obtained markedly slower estimates of the dynamics of rDNA copies (8.6 ± 2.2 and 3.4 ± 0.5 generation doubling time, respectively). Fitting single-cell GFP-LacI data, rather than the average signal displayed in Figure 2E, confirmed a median 1.5 ± 0.2 doubling time (Figures S3C and S3D). Thus, alignment of trajectories from birth or death lead to a strong and systematic underestimate of the true kinetics of the amplification of rDNA copies.

Because the chromosomal rDNA copy number is known to be tightly regulated at ~200 throughout the cell cycle (Ide et al., 2013; Mansisidor et al., 2018), we assumed that the baseline level of GFP-LacI fluorescence in the early part of the lifespan (i.e., well ahead of the SEP) is likely to correspond to chromosomal rDNA repeats, and the exponential increase in GFP-LacI fluorescence coincident with the SEP is likely due to the self-replication of ERCs. In strong support of this, the GFP signal above baseline segregates asymmetrically between mother and daughter cells, which would be inconsistent with the equal partitioning of chromosomal rDNA (see below, Figures 5A and 5B). Along these lines, it is interesting to note that GFP-LacI fluorescence appeared in aging cells as a diffuse signal rather than as a single foci in the nucleolus (Figure 1B), which is more consistent with GFP-LacI binding to multiple ERCs throughout the nucleolus than with binding to a discrete cluster of rRNA genes in the chromosomal DNA.

To better characterize the specific kinetics of ERC accumulation in mother cells, we subtracted the baseline GFP-LacI fluorescence signal (assuming it corresponded to 200 chromosomal rDNA copies), calculated the number of gene copies represented by the remaining GFP-LacI signal, and plotted the data in semi-log scale (Figure 1E, inset). This analysis confirmed the striking exponential increase in ERCs over about 15 generations, followed by a plateau representing saturation of the amplification process at ~1,500 ERC copies/cell, which is an order of magnitude higher than the chromosomal rDNA copy number and could be underestimated due to the potential titration of GFP-LacI. Importantly, extrapolating the exponential fit allowed us to estimate that the first ERC excision (defined by ERC copy number equal to 1; Figure 1E, inset) occurred an average of about 13 divisions before the SEP, i.e., long before any decline in physiological function is manifest. In addition, the number of ERCs at the SEP was ~360, indicating that aging cells can tolerate a large increase in extra rDNA copies before cell division is perturbed (Figure 1E, inset). Taken together, these results provide direct evidence for the exponential accumulation of ERCs in the mother cell and demonstrate that it is an early event that precedes by far the onset of SEP that characterizes entry into replicative senescence.

### ERC Accumulation Leads to a Massive Increase in Pre-rRNA Levels Prior to Entry into Senescence

ERCs have long been speculated to be toxic to aging cells by titrating the DNA replication machinery and/or rDNA-specific

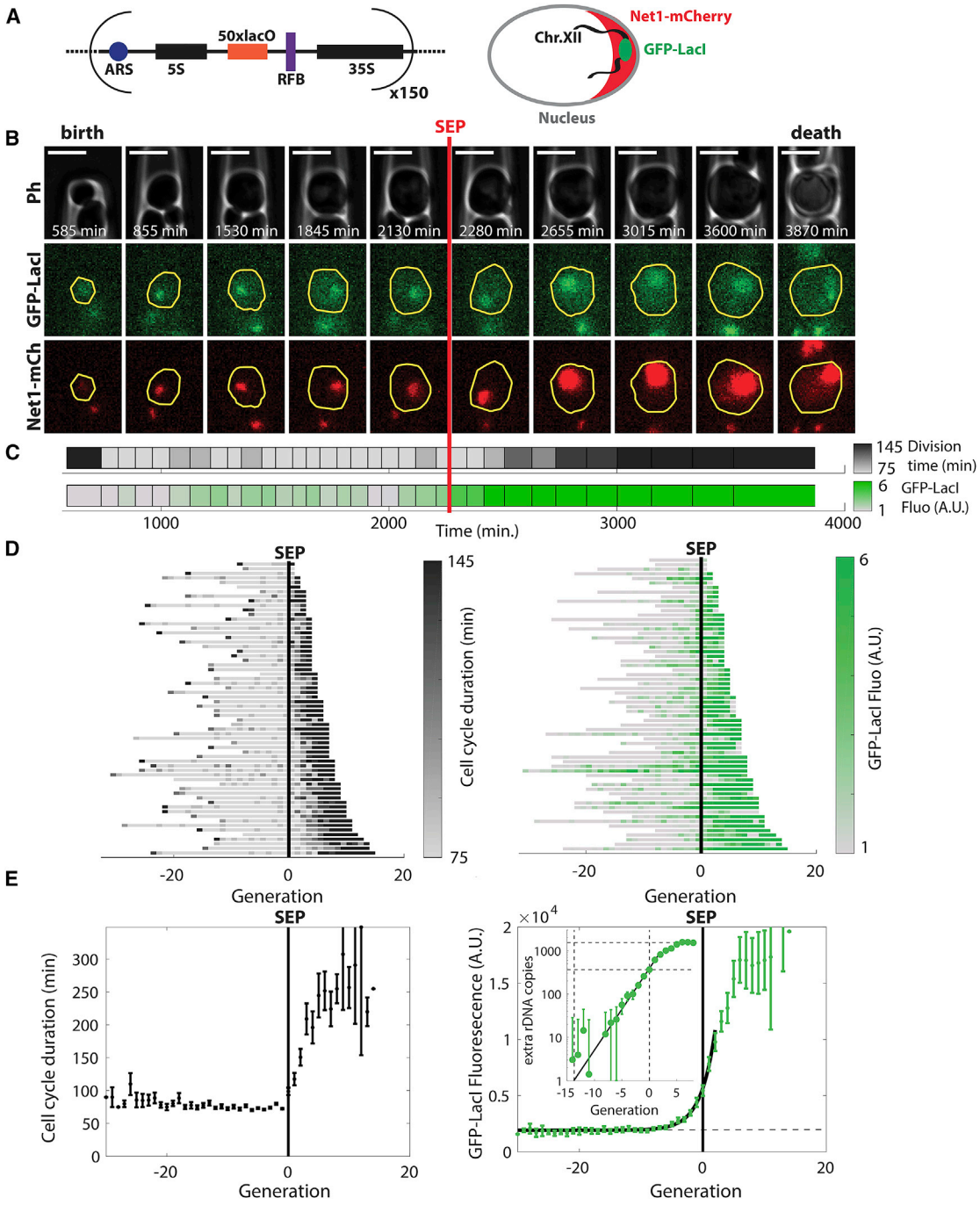


**Figure 1. rDNA Copy Numbers (ERCs) Increase Exponentially before Entry into Senescence**

(A) Schematic showing LacO insertion into each rDNA repeat in TMY8-BY4B strain also co-expressing GFP-LacI and Net1-mCherry.

(B) Phase contrast (top), GFP-LacI fluorescence (middle), and Net1-mCherry fluorescence (bottom) images of a mother cell trapped in a cavity of the microfluidic device from birth to death. The mother cell is delimited by yellow contours. Scale bars: 5 μm.

(C) Schematic showing trajectory of cell cycle duration (gray scale) and GFP-LacI signal (green scale). Black and green density is proportional to the cell cycle duration and nucleolar GFP-LacI fluorescence (rDNA copy number), respectively, for the cell shown in (B).

(D) Single-cell trajectories of cell cycle duration (left) and nucleolar GFP-LacI fluorescence (right) shown as a function of age. Trajectories are aligned to the SEP (black vertical bar).

(E) Cell cycle duration (left) and nucleolar GFP-LacI fluorescence (right) in SEP-aligned cells as a function of age. Inset: Number of presumptive extrachromosomal rDNA (ERCs) as a function of age, calculated from the GFP-LacI signal. The plot shows the exponential rise in ERC number preceding the SEP. N = 64 mother cells. Data are represented as mean ± SEM.

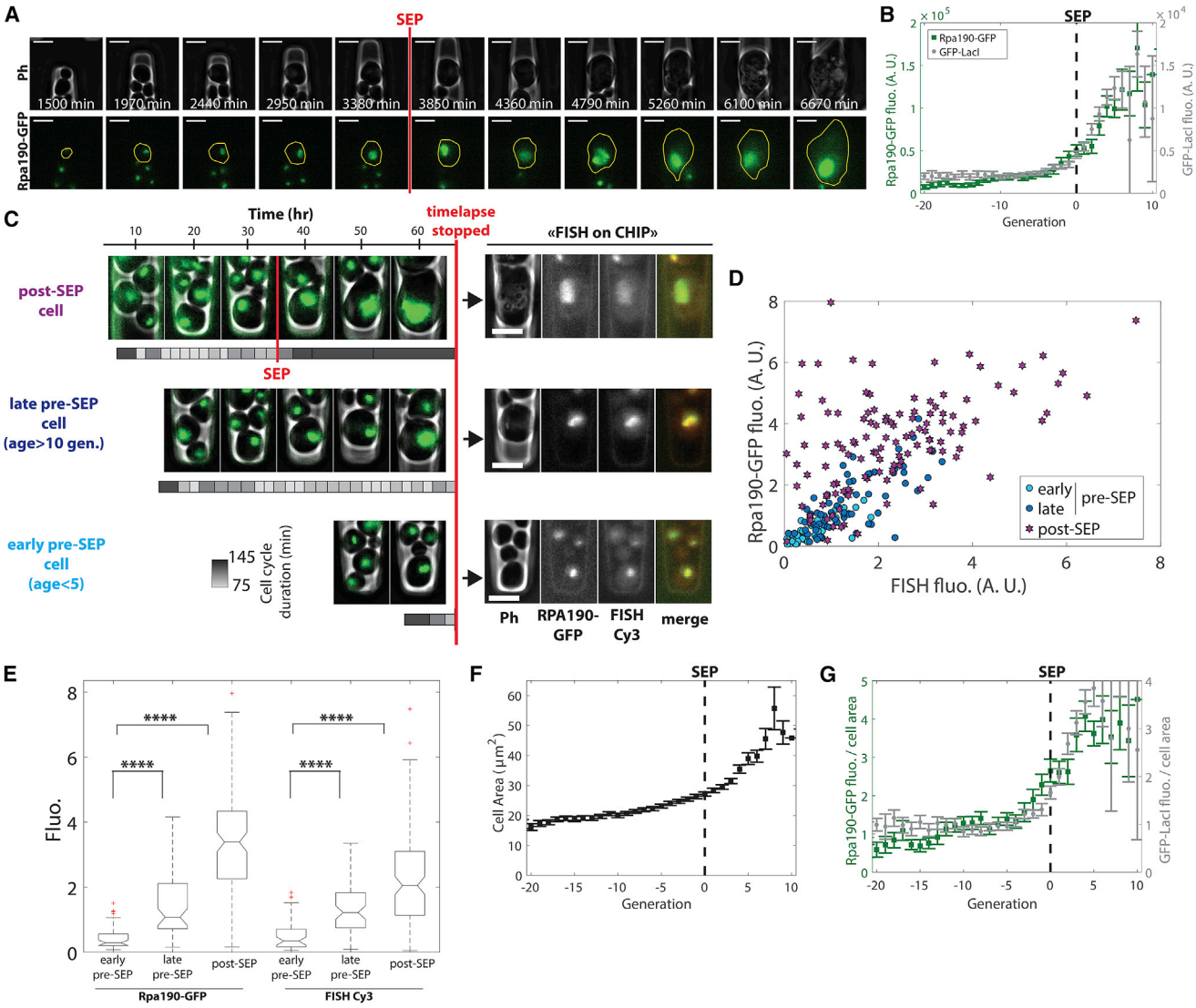


**Figure 2. Pre-rRNAs Accumulate Concomitantly with ERCs before Entry into Senescence**

(A) Phase contrast and GFP fluorescence micrographs of an Rpa190-GFP-expressing mother cell. The mother cell is delimited by yellow contours.

(B) Total Rpa190-GFP fluorescence (N = 61 cells) and nucleolar GFP-LacI fluorescence (N = 64 cells) in SEP-aligned cells as a function of age.

(C) FISH-on-CHIP. Left: Three examples of Rpa190-GFP-expressing cells tracked for different generation times before RNA FISH labeling. The number of divisions and their durations are represented in trajectories (gray scale) below the corresponding images for each cell tracked. Right: Cells shown on the left were subjected to FISH with a Cy3-tagged probe detecting all pre-rRNAs.

(D) Rpa190-GFP fluorescence as a function of FISH-Cy3 fluorescence for early pre-SEP (N = 45, light blue), late pre-SEP (N = 68, dark blue), and post-SEP (N = 123, magenta) cells.

(E) Rpa190-GFP and FISH-Cy3 fluorescence for the cells shown in (D).

(F) Cell area calculated from SEP-aligned Rpa190-GFP-expressing mother cells as a function of age (N = 61).

(G) Total Rpa190-GFP fluorescence (green) and nucleolar GFP-LacI (gray) normalized to the cell area of SEP-aligned cells plotted as a function of age.

Scale bars: 5 μm for all images. Data are represented as mean ± SEM except in (E), which are medians. ****p < 0.0001, t-test.

RNA polymerase 1 (Pol I) (Defossez et al., 1998; Denoth Lippuner et al., 2014a); however, the latter has never been experimentally verified. Here, we tested this hypothesis by examining Pol I and rDNA transcription levels.

To assess Pol I levels throughout the cell lifespan, we monitored cells expressing a fusion protein of GFP and Rpa190, the largest subunit of Pol I. Unexpectedly, we observed a large increase in total Rpa190-GFP fluorescence levels, starting before the SEP and continuing to death (Figures 2A and 2B; Video S2). By the end of the lifespan, the average Rpa190-GFP fluorescence reached a level approximately 10-fold higher than that in young cells, which paralleled the dynamics of ERC accumulation (Figure 2B). This finding suggests that, in contrast to the titration hypothesis, Pol I level may not be a limiting factor of

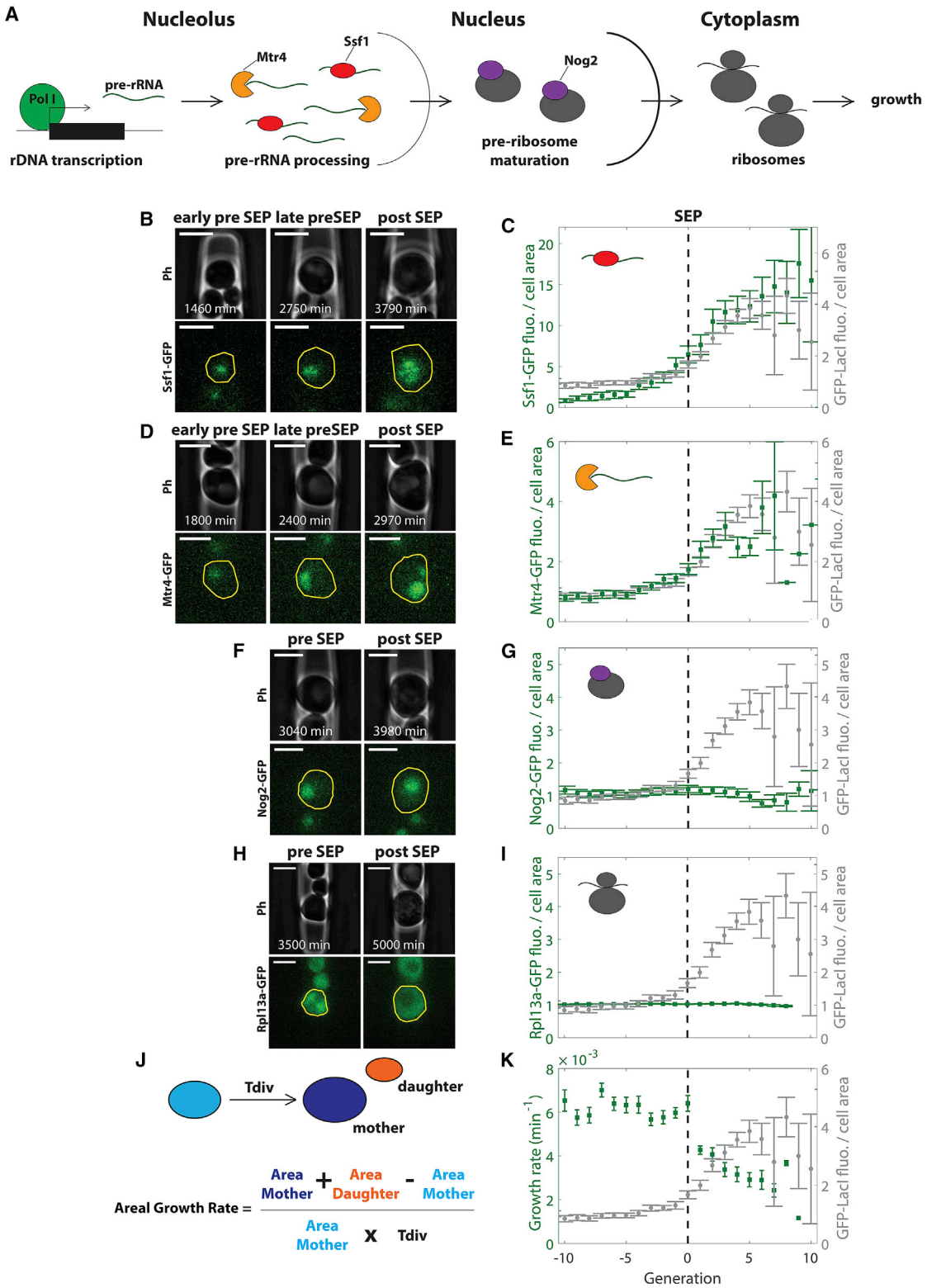


**Figure 3. Early and Late Steps of Ribosome Biogenesis Are Uncoupled before Entry into Senescence**

(A) Schematic of the steps involved in ribosome biogenesis.

(B) Phase contrast and fluorescence micrographs of an Ssf1-GFP-expressing mother cell at early and late pre-SEP and post-SEP stages.

*(legend continued on next page)*

rDNA transcription in aging cells because it increases alongside ERCs in a stoichiometric manner.

To directly assess rDNA transcription, we developed a fluorescence *in situ* hybridization protocol to measure total pre-rRNA levels in cells growing in the microfluidic chip cavities (fluorescence *in situ* hybridization [FISH]-on-CHIP). After monitoring Rpa190-GFP-expressing mother cells for 65 h, RNA FISH was performed using a 35S RNA-targeting probe sequence that labels all nucleolar pre-rRNAs from 35S to 20S. Because mother cell birth was not synchronized in all cavities, we used the history of cell division to classify the cells as in pre-SEP or post-SEP stages when RNA FISH was performed (Figure 2C). Using this methodology, we found that the RNA FISH and Rpa190-GFP fluorescence signals were not only colocalized (Figure 2C) but also correlated quantitatively (Figure 2D), albeit less strongly in post-SEP compared with pre-SEP cells (Pearson correlation coefficients = 0.5 and 0.8, respectively; Figure 2D). This result clearly indicated that the high amount of Pol I is functional and effectively produces increased levels of pre-rRNA. Moreover, based on the assumption that pre-SEP cells that achieved a larger number of generations are more likely to be close to the SEP, we further discriminated between early pre-SEP cells (<5 generations from birth) and late pre-SEP cells (>10 generations). Using this distinction, we confirmed that the increase in pre-rRNA levels preceded the SEP and coincided with the increase in Pol I levels (Figure 2E) and, thus, with the timing of ERC accumulation (Figure 2B).

To rule out the possibility that the observed upregulation in pre-rRNA levels simply reflected the characteristic increase in cell size over the lifespan (Figure 2F), we normalized Rpa190-GFP signal to cell area. The kinetics of Pol I accumulation were comparable with or without normalization to cell area (Figure 2B versus Figure 2G), confirming that pre-rRNA levels accumulate before senescence independently of cell growth. Therefore, unless specified otherwise, all of the following fluorescence data were normalized by cell area.

To sum up, the comparable scale and timings of increase in ERC and pre-RNA levels suggest that the large excess in rDNA transcription is fueled by ERC accumulation.

## Increased rDNA Transcription Prior to Entry into Senescence Is Uncoupled from Ribosome Production and Compromises Growth Homeostasis

Given the striking increase in pre-rRNAs before the SEP, we next asked whether ribosome biogenesis was also elevated in these cells and its consequence for the cellular growth rate. Therefore, we used a series of fluorescent reporter proteins to investigate whether successive steps from pre-rRNA processing to ribosome assembly were coordinated with the increase in pre-rRNA levels (Figure 3A).

To quantify pre-rRNA processing, we expressed a GFP fusion protein with Ssf1, which is a component of 66S pre-ribosomal particles that contain functionally processed rRNAs (Fatica et al., 2002). Monitoring of Ssf1-GFP fluorescence throughout the lifespan revealed similar dynamics to that of GFP-LacI (Figures 3B and 3C; Video S3). As a second pre-rRNA processing proxy, we monitored Mtr4, which is a component of the nuclear exosome required for RNA degradation during pre-rRNA processing (de la Cruz et al., 1998). Interestingly, Mtr4-GFP fluorescence also increased when the cells went through the SEP transition (Figures 3D and 3E). These data, therefore, indicate that components of the pre-rRNA maturation machinery were concomitantly upregulated with Pol I, suggesting that the increase in pre-rRNA levels was due to increased rDNA transcription rather than a defect in pre-rRNA processing.

To monitor the later steps associated with pre-ribosome nuclear export, we used a Nog2-GFP fusion protein. Nog2 is required for the nucleoplasmic steps of pre-60S maturation (Baßler et al., 2001; Saveanu et al., 2001), and its expression level is assumed to mirror the export rate. However, in contrast to the dynamics of Rpa190, Ssf1, and Mtr4, we found that the total nuclear Nog2-GFP signal (normalized to cell area) was remarkably stable throughout the cellular lifespan (Figures 3F and 3G; Video S4). Moreover, the average total ribosome content (normalized to cell area), monitored using GFP-fused Rpl13a, a component of the 60S ribosomal subunit, was also maintained at a near constant level until cell death (Figures 3H and 3I; Video S5). Taken together, these data indicate that the abundance of components of the late nuclear steps of ribosome biogenesis was relatively unaffected by cell age, suggesting that the pre-SEP excess in rDNA transcription does not lead to more ribosome assembly. Because ribosome biogenesis is finely tuned to support cell growth under physiological conditions, we hypothesized that the lack of coordination between rDNA transcription and ribosome biogenesis might be detrimental to growth in the post-SEP part of the cellular lifespan. Consistent with this, the cell growth rate actually declined in post-SEP (Figures 3J and 3K), confirming that the failure to coordinate rDNA transcription and ribosome assembly could be deleterious to cell growth.

## A Loss of Nuclear Homeostasis Drives the Decline in Cellular Physiology in Post-SEP Cells

The observation of a dramatic increase in nucleolar size, which is likely to originate from the accumulation of pre-RNAs prior to

(C) Ratios of Ssf1-GFP fluorescence (green, N = 56 cells) and GFP-LacI fluorescence (gray, N = 64 cells) to cell area in SEP-aligned cells as a function of age.
(D and E) Same as (B) and (C), respectively, for Mtr4-GFP-expressing cells (N = 40 cells).
(F and G) Same as (B) and (C), respectively, except for pre-SEP and post-SEP Nog2-GFP-expressing cells (N = 33 cells).
(H and I) Same as (B) and (C), respectively, except for Rpl13a-GFP-expressing cells (N = 32 cells).
(J) Schematic showing calculation of growth rate based on segmented contouring of the mother cells before (light blue) and after (dark blue) division and the newborn daughter (orange).
(K) Growth rate (green, measured as in J, N = 36 cells) and ratio of GFP-LacI fluorescence to cell area (gray, N = 64 cells) of SEP-aligned mother cells as a function of age.
Scale bars: 5 μm for all images. Data are represented as mean ± SEM.

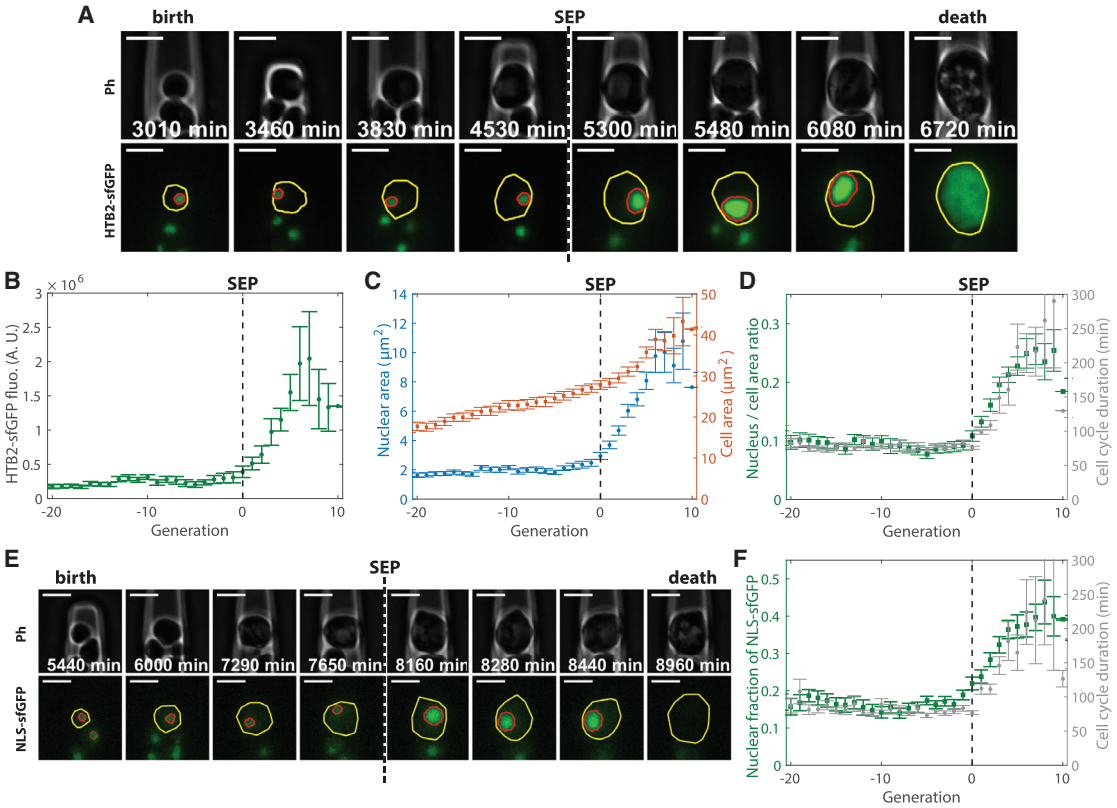


**Figure 4. Loss of Nuclear Homeostasis Occurs Concomitantly with Entry into Senescence**

(A) Phase contrast and fluorescence micrographs of a mother cell expressing the nuclear marker Htb2-sfGFP.

(B) Total Htb2-sfGFP fluorescence in SEP-aligned cells as a function of age. (N = 23 cells).

(C) Nuclear area (left axis [blue]) and cellular area (right axis [red]) of SEP-aligned cells as a function of age. (N = 23 cells).

(D) Ratio of the nuclear to cell area (left axis [green]) and cell cycle duration (right axis [gray]) of SEP-aligned cells as a function of age. (N = 23 cells).

(E) Phase contrast and fluorescence micrographs of a mother cell expressing NLS-sfGFP.

(F) Fraction of NLS-sfGFP fluorescence localized to the nucleus (left axis [green]) and cell cycle duration (right axis [gray]) in SEP-aligned cells as a function of age (N = 24 cells).

Scale bar: 5 μm for all images. Data are represented as mean ± SEM.

the SEP, prompted us to investigate how it may be linked to the subsequent decline in cell division rate. To this end, we wondered whether the overall nuclear size scales with that of the nucleolus in aging mothers. We used the histone 2B reporter Htb2-sfGFP as a nuclear reporter (Figure 4A; Video S6). Strikingly, this analysis revealed an important increase in total histone levels, the onset of which was concomitant with the SEP. Similarly, the cells underwent a dramatic increase in nuclear area (the nuclear contours were delineated using the Htb2-sfGFP marker), which could not be attributed to the age-dependent increase in cell size (Figure 4C). Indeed, the nucleus-to-cell area ratio (N/C ratio), which was remarkably stable before the SEP despite a progressive increase in cellular size, went up by about 150% in post-SEP cells (Figure 4D; Video S6) (Rempel et al., 2019). This result was unexpected knowing that the N/C ratio is tightly regulated and is relatively unaffected by mutations that perturb either cell cycle progression or cell size (Jorgensen et al., 2007; Kume et al., 2017; Neumann and Nurse, 2007). In addition, we noticed the increase in N/C ratio was clearly posterior to pre-SEP increase in rDNA transcription and ERC accumulation and, yet, was strikingly identical to the evolution of the cell cycle duration (Figure 4D). This suggests a direct relationship between dysregulation of nuclear size and the onset of physiological decline.

To check whether other proteins targeted to the nucleus would tend to undergo an increased accumulation in the nucleus after the SEP, we investigated the localization of sfGFP proteins fused with a nuclear localization signal (NLS-sfGFP) (Figure 4E). The fraction of NLS-sfGFP localized to the nucleus increased considerably as the cells passed the SEP (from 14% to 40%; Figure 4F). This increase was not due to an upregulation of NLS-sfGFP expression with age, as the total cellular fluorescence of sfGFP was almost identical throughout cellular lifespan with or without NLS (Figures S4A and S4B). These results suggested that nuclear transport was dramatically affected by age, in agreement with a recent study (Rempel et al., 2019). Altogether, these results clearly unravel a loss in nuclear homeostasis in post-SEP cells characterized by an enlargement of the nucleoplasm and the accumulation of nuclear proteins, which quantitatively coincides with the decline in cellular function.

## Asymmetrical Nuclear and Nucleolar Division Enables the Rejuvenation of Daughters of Senescent Mother Cells

It has long been observed that ERCs are primarily inherited by mother cells upon nuclear division (Sinclair and Guarente, 1997), and this asymmetrical inheritance is thought to drive daughter cell rejuvenation (Kennedy et al., 1994). However, neither asymmetrical partitioning of ERCs nor rejuvenation of daughter cells has been demonstrated by live single-cell tracking.

To address this, we examined the fate of the GFP-LacI fluorescence signal in aging mother cells upon nuclear division. Although GFP-LacI was equally partitioned into the daughter cells of young (i.e., pre-SEP) mothers, the fluorescence signal was disproportionately retained by older (i.e., post-SEP) mothers, and the daughters exhibited only basal GFP-LacI levels, consistent with asymmetrical segregation of ERCs (Figures 5A and 5B) (Shcheprova et al., 2008). This further confirms that the increase in rDNA copies observed in aged mothers is due to an accumulation of ERCs rather than to an expansion of the chromosomal rDNA array, which would be inherited by daughters.

To determine whether the recovery of basal ERC levels was associated with a recovery of physiological function in daughters, we examined their cell cycle duration. The first division time of yeast cells is highly dependent on cell volume (Hartwell and Unger, 1977), which varies considerably with age (Figure 2F); therefore, we began monitoring from the second cell division (i.e., the first division of the daughter cell as a mother; Figure 5C). We observed that the cell cycle duration of daughter cells was comparable to that of pre-SEP mother cells (Figure 5D), suggesting that the deleterious hallmarks of aging are not inherited by the daughter cells.

Therefore, to further investigate whether daughters were born clear of the other aging markers identified in this study, we examined the nucleolar size (Figure 5E), Pol I levels (Rpa190-GFP; Figures 5F and 5G), N/C ratio (Figures 5H and 5I), and Ssf1-GFP fluorescence levels (Figures S4C–S4E) of daughters born to mothers of young and old replicative ages (from 10 generations pre-SEP to 10 generations post-SEP). Notably, monitoring of each of these phenotypes over multiple generations indicated that the daughter cells displayed a rejuvenated phenotype, regardless of the age of the mother (Figures 5E–5I). These data suggest that asymmetrical partitioning of the entire nucleolus and nuclear content is involved in the rejuvenation process, thus freeing the daughters from the effects of dysregulated rDNA transcription and pre-ribosomal assembly and increased N/C ratio observed in aged mother cells.

A previous study found that daughters of very old mothers (i.e., more than 90% of the lifespan) display a very short RLS (Kennedy et al., 1994), suggesting the existence of mechanisms that limit the efficiency of the rejuvenation process, which is in contradiction with the daughter clearance of aging markers reported here. Technical limitations preclude tracking of the RLS of daughters born from post-SEP mothers within the microfluidics device. However, we observed the appearance of a multi-nucleated cell phenotype, a reflection of whole-genome instability, the frequency of which linearly increased with replicative age after the SEP (Figures 5J and 5K) (Neurohr et al., 2018). Importantly, we found that this phenotype, which is likely to be detrimental to cellular function, was faithfully inherited by daughter cells (about 60% exhibiting the multi-nucleated phenotype; Figures 5J and 5L). This observation suggests that, despite efficient epigenetic segregation of aging markers by asymmetrical nucleolar and nuclear division, mother cells are likely to undergo genetic alterations following the loss in nuclear homeostasis, which ultimately compromise daughter cell rejuvenation. Collectively, the results shown here contribute to explain the mechanism, the chronology, and the limitations associated with daughter cell rejuvenation in aging mothers.

## A Probabilistic Event Drives the Transition into Replicative Senescence

Previous work proposing that accumulation of ERCs is associated with entry into senescence is supported by the fact that *fob1Δ* mutants, which show defects in ERC excision (Defossez et al., 1999; Kobayashi, 2003; Mansisidor et al., 2018) and, hence, have lower ERC levels than wild-type (WT) cells, also have much longer lifespans (Defossez et al., 1999). Conversely, *sir2Δ* mutants, which accumulate high levels of ERCs, are relatively short-lived (Kaeberlein et al., 1999). Therefore, we asked whether and how the reduced and elevated levels of ERCs in *fob1Δ* and *sir2Δ* mutants, respectively, modified the scenario of entry into senescence described in this study.

We observed that the median lifespans of *fob1Δ* and *sir2Δ* mutants were indeed much longer and shorter, respectively, than that of WT cells (36, 13, and 29 generations, respectively; Figure 6A). Most (87%) of *sir2Δ* cells experienced a SEP prior to cell death, similarly to WT (Figures S5B and S5C). However, a detailed analysis of the trajectory of individual *fob1Δ* cells revealed that the majority (68.3%) did not undergo a slowdown in the cell cycle before death (referred to as No-SEP cells; Figures 6C and 6D) compared with only 7% of WT cells (Figure 1D). We also did not observe accumulation of GFP-LacI fluorescence during cellular lifespans of the No-SEP *fob1Δ* subpopulation (Figures 6E and 6F), which is in contrast to the remaining *fob1Δ* population that did experience the SEP (referred to as With-SEP), which displayed a similar increase in GFP-LacI (Figures 6E and 6F) and Net1-mCherry fluorescence signals (Figures S6A–S6C) as observed in WT cells.

This observation suggested that ERCs do not accumulate in No-SEP *fob1Δ* cells; therefore, they must die through an ERC-independent mechanism. To investigate this further and to establish the precise relationship between ERC levels and concomitant or downstream events, we monitored Pol I levels (using Rpa190-GFP), the N/C ratio (Htb2-GFP), and the growth rate in the No-SEP and With-SEP *fob1Δ* subpopulations. Notably, the Pol I content (Figures 6B and 6G; Video S7), N/C ratio (Figure 6H; Figure S6D), and growth rate (Figure S6F) of the No-SEP subpopulation were nearly constant throughout the lifespan, whereas the phenotypes of the With-SEP *fob1Δ* subpopulation and WT cells were virtually indistinguishable (Figures 6B, 6G, and 6H; Figures S6E and S6F; Video S8). A recent study suggested that excessive

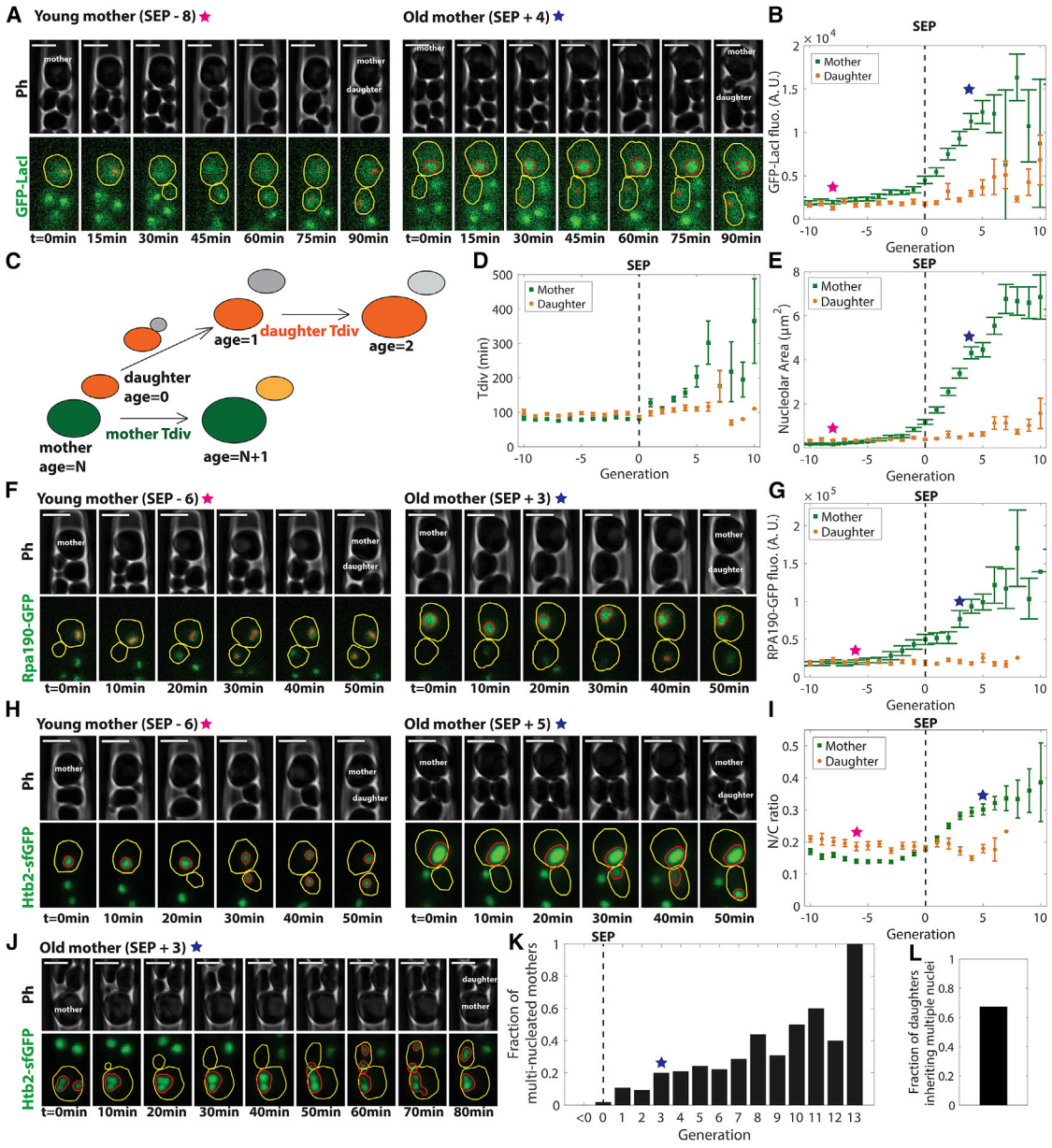


**Figure 5. Rejuvenated Daughter Cells of Aging Mothers Show Basal Levels of ERCs and Pre-rRNA Synthesis**

(A) Phase contrast and fluorescence micrographs of a dividing GFP-LacI-expressing mother cell at a young age (8 divisions before SEP, left, pink star) and at an old age (4 divisions after SEP, right, blue star).

(B) Nucleolar GFP-LacI fluorescence in SEP-aligned mother (green) and daughter (orange) cells as a function of age (N = 23–64 cells). Pink and blue stars indicate the stages corresponding to the cells shown in (A).

(C) Schematic showing calculation of the cell cycle duration for the daughter cell shown in orange.

(D) Cell cycle duration of SEP-aligned mother (green) and daughter (orange) cells as a function of age (N = 29 cells).

(E) Nucleolar area in SEP-aligned mother (green) and daughter (orange) cells as a function of age (N = 23–64 cells).

(F and G) Same as (A) and (B), respectively, except showing Rpa190-GFP fluorescence (N = 21–61 cells).

(H) Same as (A) except showing Htb2-sfGFP-expressing cells.

(I) Nuclear to cellular area (N/C) ratio in SEP-aligned mother (green) and daughter (orange) cells as a function of age (N = 42 cells).

(J) Phase-contrast and fluorescence micrographs of a multi-nucleated mother cell transmitting two nuclei to its daughter.

(K) Fraction of multi-nucleated mothers as a function of age.

(L) Fraction of daughters inheriting nuclear defects (31 of 46 cells).

Scale bars: 5 μm for all images. Data are represented as mean ± SEM.

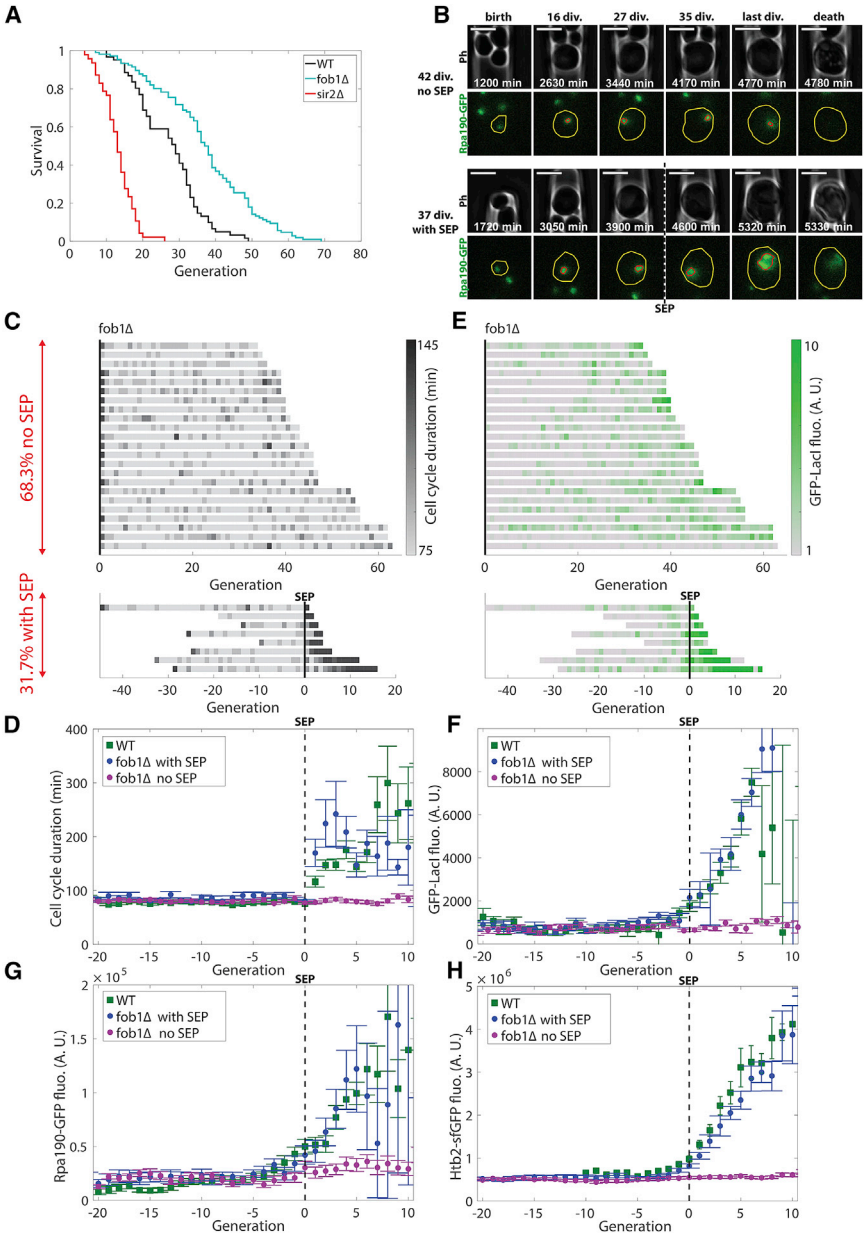


**Figure 6. Senescence Entry Is Controlled by a FOB1-Dependent Stochastic Process That Dysregulates Nucleolar Activity**

(A) Survival curves of WT cells (black, RLS = 29, N = 61), *fob1Δ* cells (cyan, RLS = 36, N = 126), and *sir2Δ* cells (red, RLS = 13, N = 55 cells).

(B) Phase-contrast and fluorescence micrographs of two Rpa190-GFP-expressing *fob1Δ* mother cells: one that never experiences a SEP (RLS = 42 generations; top) and one that experiences a SEP after 33 divisions (RLS = 37 generations; bottom). Scale bars: 5 μm.

(C) Trajectories of cell cycle durations for *fob1Δ* No-SEP (top) and With-SEP (bottom) sub-populations.

(D) Cell cycle duration of SEP-aligned WT cells (green, N = 57), With-SEP *fob1Δ* cells (blue, N = 40), and No-SEP *fob1Δ* cells (magenta, N = 84).

(E) Trajectories of GFP-LacI fluorescence for the same cells represented in (C).

(F–H) GFP-LacI (F), Rpa190-GFP (G), and Htb2-sfGFP (H) fluorescence in SEP-aligned WT cells (green), With-SEP *fob1Δ* cells (blue), and No-SEP *fob1Δ* cells (magenta). No-SEP cells were aligned from birth with generation 0 set at the median SEP of the corresponding With-SEP *fob1Δ* cells (30 for D, 25 for F, 21 for G, and 27 for H) (N = 20–61 cells). Data are represented as mean ± SEM.

cell growth could contribute to senescence by diluting cytoplasm (Neurohr et al., 2019). Although it is not excluded that this process could impair cell survival at very late stages of lifespan, cytoplasm dilution does not seem to be involved in ERC accumulation and to trigger the SEP, as cell size increased very similarly throughout the lifespan in *fob1Δ* cells (Figure S6G) despite different cell fates (With-SEP or No-SEP).

In contrast to *fob1Δ*, *sir2Δ* cells presented a shorter lifespan than WT (Figure 6A) and an early entry into senescence (Figure S5B), which is consistent with ERC accumulation being the driver of SEP. However, GFP-LacI fluorescence signal aligned at SEP exhibited very similar trends in WT and *sir2Δ* populations (Figures S5A, S5D, and S5E), suggesting that the process of exponential accumulation of ERCs is identical in *sir2Δ* and WT (doubling time, 1.9 ± 1.4 generations). Thus, the early entry into senescence observed in *sir2Δ* is likely due to a higher rate of ERC excision rather than to a faster accumulation of ERCs.

These data further support the hypothesis that ERC accumulation may contribute, at least in part, to the loss of nuclear homeostasis in aging cells. In addition, the heterogeneity in cell fate observed in the *fob1Δ* mutant suggests that the ERC-dependent entry into senescence is a stochastic process, the probability of which is greatly reduced by the *fob1Δ* mutation and increased by the *sir2Δ* mutation, and that an ERC-independent mechanism sets the subsequent limit of replicative longevity.

## A Quantitative Model of Entry into Replicative Senescence in Budding Yeast

Our results thus far support a clear order of events in the transition to replicative senescence in yeast. The probabilistic excision of an ERC leads to the exponential accumulation of rDNA copies over a multi-generation timescale and precedes the onset of SEP and loss of nuclear homeostasis that likely causes cell death (Figure 7A).

Because this interpretation derives from quantitative experimental results (ERC accumulation, cell cycle duration, and lifespan measurements), we sought to build a computational model

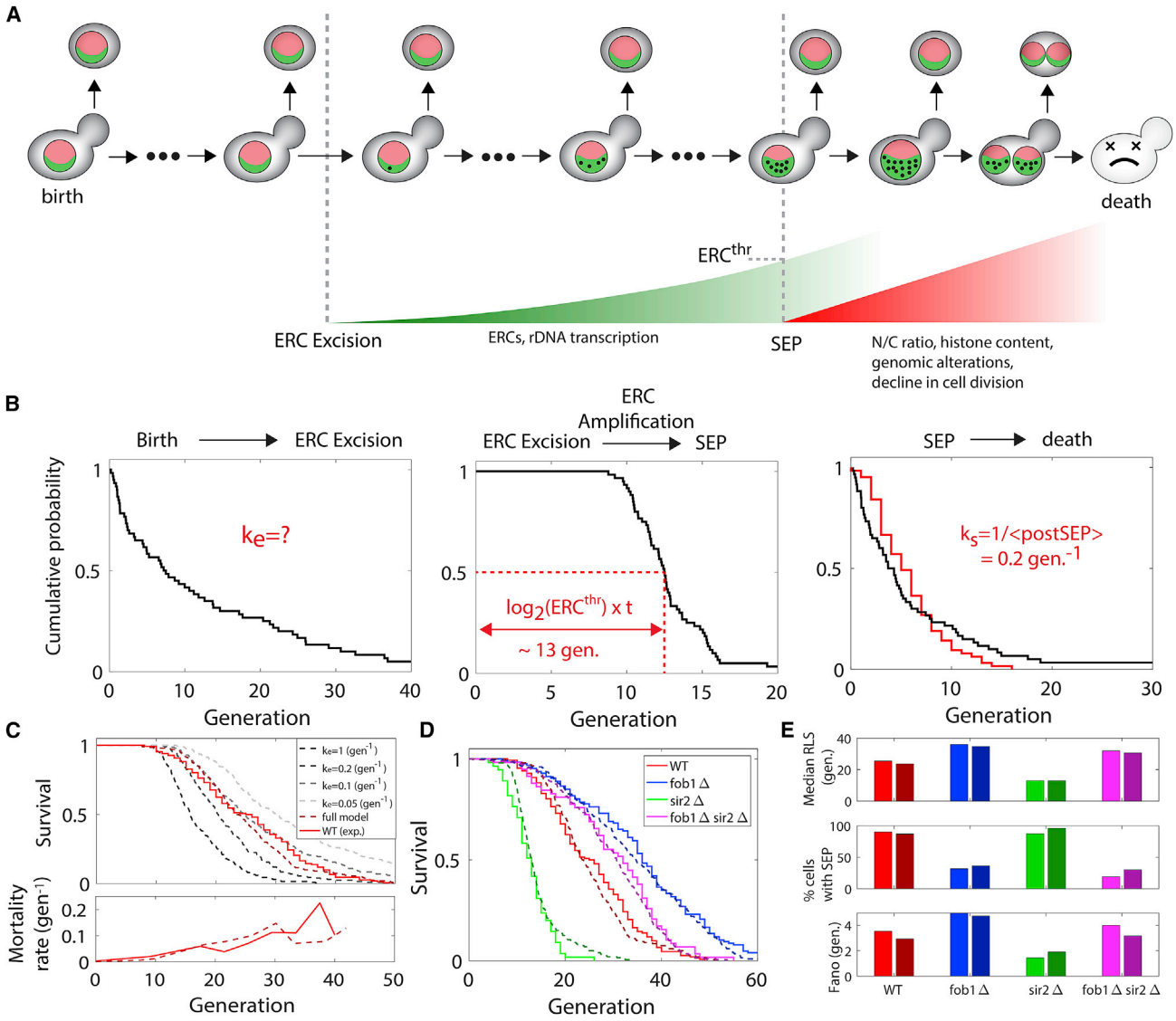


**Figure 7. Biological and Computational Model of Entry into Senescence**

(A) Schematic showing the three steps involved in ERC-dependent senescence (ERC excision, ERC self-replication, and post-SEP interval).

(B) Cumulative probability (black lines) associated with each step shown in (A), as defined by the computational model (see STAR Methods), by using experimentally determined parameter values (indicated in red; see Table S1). Left: Cumulative distribution of times from birth to the first ERC excision. Middle: Cumulative distribution of the duration of accumulation of ERCs from 1 to $ERC^{thr}$ copies. The median (red dashed line) corresponds to the experimentally measured value reported in Figure 2E. Right: Cumulative distribution of times from SEP to cell death. The red line represents the experimentally measured distribution in WT.

(C) Top: Experimentally determined RLS of WT cells (solid line) and the influence of the excision rate $k_e$ on RLS, as predicted by the computational model (gray dashed lines). The dark red line indicates the numerical RLS obtained by adding an ERC-independent cause of death (referred to as the "full model," see A Quantitative Model of Entry into Replicative Senescence in Budding Yeast). Bottom: Mortality rate (i.e., probability of live cells to die per generation) as a function of age calculated for both experimental (solid red line) and full model (red dashed line).

(D) Experimentally determined (solid lines) and computationally predicted (dashed lines) RLS for WT cells and the indicated mutants.

(E) Experimentally determined (light bars) and computationally predicted (dark bars) median RLS (top), fractions of cells experiencing a SEP (middle) and Fano factor (bottom) obtained for WT cells and each indicated mutant.

N = 200 cells for all computationally determined curves.

based on this scenario to determine whether it could recapitulate the distribution of lifespans and the fraction of cells experiencing the SEP in WT cells as well as in the mutant strains in which the ERC excision rate is perturbed.

We designed a stochastic numerical model with continuous time—inspired from a previous study (Gillespie et al., 2004)—whereby the cellular lifespan is the convolution of three steps (see Figure S7A and STAR Methods for details): the stochastic

excision of the first ERC (rate $k_e$; Figure 7B, left); the self-replication of ERCs (with a doubling time $\tau$; Figure 7B, middle) until a threshold number $ERC^{thr}$ is reached that corresponds to the SEP; and an interval between SEP and cell death, which is associated with the loss of nuclear homeostasis (rate $k_s$; Figure 7B, right).

Most parameter values could be estimated experimentally from single-cell measurements: the number of generations achieved by the cells in the post-SEP interval was close to an exponential distribution with a mean post-SEP around 5 generations (Figure 7B), in agreement with a random death rate $k_s$ = 1/(post-SEP) = 0.2 generation $(gen)^{-1}$ (Figure 7B). The ERC doubling time $\tau$ = 1.5 gen and the threshold number $ERC^{thr}$ = 360 were measured from the exponential increase in GFP-LacI fluorescence signal (Figure 1D). These two parameters set the timescale of the ERC self-replication phase, i.e., $\log_2(ERC^{thr}) \times \tau \sim 13$ generations (Figure 7B). $k_e$ was the only free parameter to fit the model to the data. Interestingly, $k_e = 0.1\ gen^{-1}$ provided good agreement with the experimental RLS in WT cells (Figure 7C, top panel), except for the prolongation of survival observed at advanced ages. Importantly, this indicates that the increased mortality with age (which is the formal definition of aging, see bottom panel on Figure 7C) can be well accounted for by the sequence of three age-independent kinetic steps. In this scenario, replicative aging appears to derive from a stochastic triggering event related to rDNA instability, the outcome of which is protracted due to the long period over which ERC amplification occurs as well as substantial cellular buffering against the deleterious consequences of ERC accumulation occurring in post-SEP. This result differs from the model of Gillespie et al. (2004), in which a quadratic increase of the probability of ERC excision with age was required to obtain a good fit to the data. The difference comes from the fact that a substantial part of the variability in survival is due to the post-SEP interval (Figure S7), which could not be taken into account in the Gillespie et al. model.

Based on this model, lowering the rate of ERC excision $k_e$ should recapitulate the lifespan extension observed in *fob1Δ* cells. However, it is much less clear how a refined model could quantitatively capture the partitioning of individual *fob1Δ* lifespans into ERC-dependent versus ERC-independent cell fates. To investigate this, we included in the model the possibility that cell death could also occur due to a competing ERC-independent cause following a standard Gompertz law (i.e., dictated by a mortality rate $\lambda$ given by $\lambda[age] = \lambda_0 \times \exp[\mu \times age]$, where $\lambda_0$ and $\mu$ are constant parameters). Assuming that the parameters associated with the Gompertz law ($\lambda_0$ and $\mu$) were identical in the *fob1Δ* mutant and WT, fitting $k_e$, $\lambda_0$, and $\mu$ to the data provided reasonable agreement with the RLS curves for WT cells ($k_e = 0.1\ gen^{-1}$) and *fob1Δ* cells ($k_e = 0.02\ gen^{-1}$) (Figure 7D), suggesting that the mutant has a 5-fold lower ERC excision rate than WT cells. Most importantly, the model also accurately captured the fraction of cells experiencing an ERC-dependent SEP in both WT and *fob1Δ* cells (Figure 7E; Figures S7B and S7C). In addition, introducing the Gompertz law improved the agreement of the model to the experimental RLS curve for WT cells by cutting the long tail in the survival curve (Figure 7C, top panel).

Conversely, we wondered under which assumption this model could capture the lifespan reduction observed in the *sir2Δ* background, which prematurely accumulates ERCs to high levels (Kaeberlein et al., 1999). A decent fit to the data required both a 20-fold higher ERC excision rate ($k_e = 2\ gen^{-1}$ in *sir2Δ* versus $0.1\ gen^{-1}$ in WT) and a 3-fold larger basal mortality rate ($\lambda_0 = 0.03\ gen^{-1}$ in *sir2Δ* versus $\lambda_0 = 0.01\ gen^{-1}$ in WT) than in WT, showing that the premature death in this mutant has multiple origins (i.e., not only ERC-dependent), as suggested previously (Kaeberlein et al., 1999). The consequence of a high rate of ERC excision was to considerably reduce the influence of the interval time between the birth and ERC excision on the total lifespan, hence reducing the cell-cell variability therein. Using the Fano factor (Fano, 1947), which provides a mean-independent measurement of heterogeneity in a distribution, we found a ~3-fold reduction in lifespan variability in the *sir2Δ* strain compared to WT, which was successfully accounted for by the model (Figure 7E; Figure S7C). Conversely, the *fob1Δ* strain displayed a marked increase in lifespan variability compared to WT (Figure 7E).

In contrast to *sir2Δ*, the experimental RLS of the *fob1Δ sir2Δ* double mutant was slightly higher than that of WT cells (Figure 7D), which is in agreement with previous studies (Kaeberlein et al., 1999, 2004). As with the *fob1Δ* strain, only a minority of double mutant cells (18%) experienced a SEP, suggesting that the ERC excision rate was similar to that of the single *fob1Δ* mutant and that the *sir2* mutation only governed the ERC-independent death rate. Indeed, a good agreement with experimental data in the double mutant was found when using a low ERC excision rate ($k_e = 0.02\ gen^{-1}$) with a high ERC-independent mortality rate, as in the *sir2Δ* mutant ($\lambda_0 = 0.03\ gen^{-1}$) (Figure S7C). Altogether, this computational model provides support for a probabilistic scenario of entry into senescence, which quantitatively explains the origin of cell-cell variability in cellular lifespan. Furthermore, it suggests that a stochastic age-independent crisis associated with rDNA instability sets the first replicative limit and that a different mechanism may set subsequent replicative limits.

## DISCUSSION

Heterogeneity in cellular lifespan within a population has long been a major impediment to understanding the mechanisms governing entry into senescence by blurring the chain of causality. In this study, we used longitudinal tracking of individual cells coupled with quantitative analysis and computational methods to propose a comprehensive description of the sequence of events leading to replicative arrest in budding yeast. Our single-cell approach strongly suggests a temporal distinction between early and later hallmarks of senescence, thereby questioning the classical view of a multifactorial aging process in which the causes and consequences of events are often reported to be tightly intertwined. Instead, our analysis establishes that ERC accumulation may drive an upregulation of rDNA transcription prior to the SEP and that entry into senescence is accompanied by a breakdown in nuclear homeostasis that is likely to trigger cell death. In this context, it appears that studies focusing on the last division preceding cell death are more likely to refine our understanding of cellular "necrology" than to explain the mechanisms that trigger replicative senescence.

Excision and accumulation of ERCs in mother cells are well-established events proposed to limit yeast lifespan (Sinclair and Guarente, 1997). A recently published study examined the cell cycle impairment during the last divisions before cell death by using the nucleolar marker Net1-mCherry as an indirect proxy for ERCs (Neurohr et al., 2018). By directly monitoring and quantifying the dynamics of rDNA copy number in living cells, throughout their whole lifespan, our study further reveals that ERCs follow a multiplicative self-replicative process with high efficiency, finally providing evidence for a long-standing but previously unverified hypothesis (Sinclair and Guarente, 1997). Then, we provide reliable estimates of the maximum number of ERCs (~360) that can be tolerated by the cell before detrimental effects ensue. The large number of ERCs accumulated by the time of death (~1,500) reveals the magnitude of the increase in rDNA content, which is comparable to the size of the entire genome (Neurohr et al., 2018; Sinclair and Guarente, 1997). The inability of cells to sustain exponential expansion of ERCs beyond the SEP might also be a hallmark of impairment of the DNA replication machinery, a hypothesis that remains to be evaluated in future studies. Finally, we show that ERC accumulation is a lengthy process initiated long before the detection of any known hallmarks of senescence (with the exception of the loss in vacuolar acidity [Hughes and Gottschling, 2012]) and the triggering signal is likely to occur about 10–15 generations before the onset of SEP, very early in life.

In addition to the hypothesis that ERCs limit RLS, it has also been proposed that rDNA instability, not ERCs themselves, drive entry into senescence (Ganley et al., 2009; Saka et al., 2013). Because we observed increased Pol I and pre-rRNA levels concomitant with the exponential accumulation of ERCs, we cannot exclude a scenario in which an unknown event that regulates chromosomal rDNA transcription initiates nucleolar stress, which then triggers ERC excision. However, in this case, it would be difficult to explain why the range of nucleolar markers examined here would all display sustained exponential kinetics of accumulation over close to 20 generations. Instead, this phenomenon seems easier to conceive if it is being driven by accumulation of self-replicating ERCs. In addition, a stochastic event, like ERC excision, can better explain the two subpopulations No-SEP and With-SEP emerging from an isogenic population growing in a well-controlled environment.

Under physiological conditions, the rate of rDNA transcription is buffered against variations in rDNA copy numbers (Dammann et al., 1993; French et al., 2003; Takeuchi et al., 2003). Based on this, it is usually assumed that increasing rDNA copies beyond physiological numbers (as in the case of ERCs here) should not impact on rDNA transcription rates. In that case, accumulating ERCs should not be transcribed. In contrast to this reasoning, we show that levels of pre-rRNAs and components of the rDNA transcription machinery are massively increased in cells about to enter senescence. This invalidates the assumption that rDNA transcription is under precise homeostatic regulation around the SEP and suggests that ERCs fuel excessive rDNA transcription in a mechanism that remains to be determined. Our study demonstrates that, despite a large increase in pre-rRNA synthesis and processing, senescent cells are unable to scale up ribosome production. This lack of coordination between RNA synthesis and ribosome biogenesis is consistent with a previous study showing that transcription and translation of genes involved in protein biogenesis are uncoupled in aging cells (Janssens et al., 2015).

Recent studies have uncovered mechanistic links between aging and a number of physiological defects in nuclear processes, including the accumulation of nuclear pores (Denoth Lippuner et al., 2014b), their functional decline (Rempel et al., 2019), and the dysregulation of cell cycle controllers such as the transcriptional repressor Whi5 (Neurohr et al., 2018). Our study revealed that entry into senescence is associated with a large increase in the N/C ratio and an overall accumulation of proteins targeted to the nucleus, thus raising the possibility of defective protein shuttling across the nucleus (Kume et al., 2017). The finding that nucleolar stress precedes the defects in protein shuttling suggests a possible causal relationship; for example, nuclear pores may become clogged by a buildup of pre-RNAs or ERCs, as proposed previously (Denoth Lippuner et al., 2014b).

Our study provides insights into the mechanism of daughter cell rejuvenation by demonstrating, in single cells, that asymmetrical nucleolar and nucleoplasmic partitioning in post-SEP mother cells correlates with the rejuvenation of daughter cells. This observation provides further support to the model in which asymmetrical inheritance of ERCs accumulating in the nucleolus is a driver of the rejuvenation process. Similarly to autonomously replicating DNA circles, the asymmetrical nucleolar and nuclear division could be due to the diffusion barrier at the bud neck (Shcheprova et al., 2008). However, our results also reveal that genomic defects present in post-SEP mothers are largely inheritable and are likely to prevent full recovery of the RLS in daughter of very old mothers, which has been reported long ago (Kennedy et al., 1994). Therefore, our study reconciles the epigenetic paradigm of daughter rejuvenation (i.e., daughters do not inherit the age of their mother) with the long-standing observation that old cells accumulate genomic alterations that must be inherited by the progeny (McMurray and Gottschling, 2003).

The nucleolar stress described in this study is likely conserved across species because similar observations have been reported in several studies in metazoans. In mouse embryonic fibroblasts, oncogenic stress induces rRNA transcription and triggers cellular senescence (Nishimura et al., 2015). Human fibroblasts were shown to accumulate rRNA precursors in the nucleolus and display defective ribosome biogenesis after induction of senescence by oncogenic *Ras* (Lessard et al., 2018). More recently, maintenance of nucleolar homeostasis was shown to alleviate senescence in human mesenchymal stem cells (Ren et al., 2019). Similarly, small nucleoli in post-mitotic cells were found to be a hallmark of extended longevity in *Caenorhabditis elegans*, *Drosophila*, mice, and human muscle tissue (Tiku et al., 2017). These results, together with the findings here, uncover a crucial role for the nucleolus in both replicative and chronological aging, suggesting that mechanisms ensuring rDNA stability are key regulators of longevity.

Finally, our computational model proposes a simple yet quantitative description of the steps leading to entry into senescence. Based on the main assumptions that excision and amplification of ERCs control the onset of SEP, we can recapitulate the RLS in WT cells and in a number of mutants in which

the rate of ERC excision is affected. Most importantly, this kinetic model of cellular lifespan is based on age-independent steps and fully supports a model in which senescence in budding yeast is driven by a purely stochastic event associated with rDNA instability, the physiological consequences of which are protracted due to the kinetics of ERC accumulation. Further experiments could further challenge this model. For example, inducing ERCs in the NO-SEP *fob1Δ* population should be sufficient to trigger the whole cascade of events (accumulation of pre-rRNAs, SEP, and loss of nuclear homeostasis). This scenario reveals how the process of aging—which manifests as an increase in the mortality rate—might be seen as an emerging property driven by a series of age-independent biological processes.

## STAR★METHODS

Detailed methods are provided in the online version of this paper and include the following:

- KEY RESOURCES TABLE
- LEAD CONTACT AND MATERIALS AVAILABILITY
- EXPERIMENTAL MODEL AND SUBJECT DETAILS
- METHOD DETAILS
  - Yeast strains, plasmids, and media
  - Microfluidics
  - RNA FISH-on-a-CHIP
  - Time-lapse microscopy
  - Image analysis
  - Data analysis
  - Computational simulations of replicative lifespan
- QUANTIFICATION AND STATISTICAL ANALYSIS
- DATA AND CODE AVAILABILITY

### SUPPLEMENTAL INFORMATION

Supplemental Information can be found online at https://doi.org/10.1016/j.celrep.2019.06.032.

### ACKNOWLEDGMENTS

We thank Denis Fumagalli and the MEDIAPREP facility of IGBMC for preparing media and Prof. Takehiko Kobayashi for providing the TMY8 strain. We are grateful to Theo Aspert, Renee Chow, Basile Jacquel, Alastair McEwen, Manuel Mendoza, Sophie Quintin, and Zhou Xu for careful reading of the manuscript. This work was supported by the ATIP-Avenir program 2012-2017 (G.C.), a grant from the Fondation pour la Recherche Médicale FRM DEI20151234397 (G.C.), and by grant ANR-10-LABX-0030-INRT, a French State fund managed by the Agence Nationale de la Recherche under the frame program Investissements d'Avenir ANR-10-IDEX-0002–02. This work was partly supported by the French RENATECH network.

### AUTHOR CONTRIBUTIONS

S.M., Conceptualization, Data curation, Formal analysis, Investigation, Visualization, Methodology, Project administration, Supervision, Writing— original draft. J.S., Data curation, Formal analysis, Investigation. I.L.-S., Methodology, Conceptualization. A.M., Resources. O.G., Conceptualization. G.C., Conceptualization, Formal analysis, Methodology, Visualization, Project administration, Software, Supervision, Funding acquisition, Writing— review & editing.

### DECLARATION OF INTERESTS

The authors declare no competing interests.

Received: February 11, 2019
Revised: April 9, 2019
Accepted: June 7, 2019
Published July 9, 2019

### REFERENCES

Baßler, J., Grandi, P., Gadal, O., Lessmann, T., Petfalski, E., Tollervey, D., Lechner, J., and Hurt, E. (2001). Identification of a 60S preribosomal particle that is closely linked to nuclear export. Mol. Cell *8*, 517–529.

Brewer, B.J., and Fangman, W.L. (1988). A replication fork barrier at the 3′ end of yeast ribosomal RNA genes. Cell *55*, 637–643.

Dammann, R., Lucchini, R., Koller, T., and Sogo, J.M. (1993). Chromatin structures and transcription of rDNA in yeast *Saccharomyces cerevisiae*. Nucleic Acids Res. *21*, 2331–2338.

de la Cruz, J., Kressler, D., Tollervey, D., and Linder, P. (1998). Dob1p (Mtr4p) is a putative ATP-dependent RNA helicase required for the 3′ end formation of 5.8S rRNA in Saccharomyces cerevisiae. EMBO J. *17*, 1128–1140.

Defossez, P.-A., Park, P.U., and Guarente, L. (1998). Vicious circles: a mechanism for yeast aging. Curr. Opin. Microbiol. *1*, 707–711.

Defossez, P.-A., Prusty, R., Kaeberlein, M., Lin, S.-J., Ferrigno, P., Silver, P.A., Keil, R.L., and Guarente, L. (1999). Elimination of replication block protein Fob1 extends the life span of yeast mother cells. Mol. Cell *3*, 447–455.

Denoth Lippuner, A., Julou, T., and Barral, Y. (2014a). Budding yeast as a model organism to study the effects of age. FEMS Microbiol. Rev. *38*, 300–325.

Denoth-Lippuner, A., Krzyzanowski, M.K., Stober, C., and Barral, Y. (2014b). Role of SAGA in the asymmetric segregation of DNA circles during yeast ageing. eLife *3*, e03790.

Egilmez, N.K., and Jazwinski, S.M. (1989). Evidence for the involvement of a cytoplasmic factor in the aging of the yeast Saccharomyces cerevisiae. J. Bacteriol. *171*, 37–42.

Erjavec, N., Larsson, L., Grantham, J., and Nyström, T. (2007). Accelerated aging and failure to segregate damaged proteins in Sir2 mutants can be suppressed by overproducing the protein aggregation-remodeling factor Hsp104p. Genes Dev. *21*, 2410–2421.

Fano, U. (1947). Ionization Yield of Radiations. II. The Fluctuations of the Number of Ions. Phys. Rev. *72*, 26–29.

Fatica, A., Cronshaw, A.D., Dlakić, M., and Tollervey, D. (2002). Ssf1p prevents premature processing of an early pre-60S ribosomal particle. Mol. Cell *9*, 341–351.

Fehrmann, S., Paoletti, C., Goulev, Y., Ungureanu, A., Aguilaniu, H., and Charvin, G. (2013). Aging yeast cells undergo a sharp entry into senescence unrelated to the loss of mitochondrial membrane potential. Cell Rep. *5*, 1589–1599.

French, S.L., Osheim, Y.N., Cioci, F., Nomura, M., and Beyer, A.L. (2003). In exponentially growing Saccharomyces cerevisiae cells, rRNA synthesis is determined by the summed RNA polymerase I loading rate rather than by the number of active genes. Mol. Cell. Biol. *23*, 1558–1568.

Ganley, A.R., Ide, S., Saka, K., and Kobayashi, T. (2009). The effect of replication initiation on gene amplification in the rDNA and its relationship to aging. Mol. Cell *35*, 683–693.

Garmendia-Torres, C., Tassy, O., Matifas, A., Molina, N., and Charvin, G. (2018). Multiple inputs ensure yeast cell size homeostasis during cell cycle progression. eLife *7*, e34025.

Gillespie, D.T. (1977). Exact stochastic simulation of coupled chemical reactions. J. Phys. Chem. *81*, 2340–2361.

Gillespie, C.S., Proctor, C.J., Boys, R.J., Shanley, D.P., Wilkinson, D.J., and Kirkwood, T.B.L. (2004). A mathematical model of ageing in yeast. J. Theor. Biol. *229*, 189–196.

Goulev, Y., Morlot, S., Matifas, A., Huang, B., Molin, M., Toledano, M.B., and Charvin, G. (2017). Nonlinear feedback drives homeostatic plasticity in $H_2O_2$ stress response. eLife *6*, e23971.

Hartwell, L.H., and Unger, M.W. (1977). Unequal division in *Saccharomyces cerevisiae* and its implications for the control of cell division. J. Cell Biol. *75*, 422–435.

Hughes, A.L., and Gottschling, D.E. (2012). An early age increase in vacuolar pH limits mitochondrial function and lifespan in yeast. Nature *492*, 261–265.

Huh, W.K., Falvo, J.V., Gerke, L.C., Carroll, A.S., Howson, R.W., Weissman, J.S., and O'Shea, E.K. (2003). Global analysis of protein localization in budding yeast. Nature *425*, 686–691.

Ide, S., Saka, K., and Kobayashi, T. (2013). Rtt109 prevents hyper-amplification of ribosomal RNA genes through histone modification in budding yeast. PLoS Genet. *9*, e1003410.

Janssens, G.E., Meinema, A.C., González, J., Wolters, J.C., Schmidt, A., Guryev, V., Bischoff, R., Wit, E.C., Veenhoff, L.M., and Heinemann, M. (2015). Protein biogenesis machinery is a driver of replicative aging in yeast. eLife *4*, e08527.

Jorgensen, P., Edgington, N.P., Schneider, B.L., Rupes, I., Tyers, M., and Futcher, B. (2007). The size of the nucleus increases as yeast cells grow. Mol. Biol. Cell *18*, 3523–3532.

Kaeberlein, M., McVey, M., and Guarente, L. (1999). The SIR2/3/4 complex and SIR2 alone promote longevity in Saccharomyces cerevisiae by two different mechanisms. Genes Dev. *13*, 2570–2580.

Kaeberlein, M., Kirkland, K.T., Fields, S., and Kennedy, B.K. (2004). Sir2-independent life span extension by calorie restriction in yeast. PLoS Biol. *2*, E296.

Kennedy, B.K., Austriaco, N.R., Jr., and Guarente, L. (1994). Daughter Cells of *Saccharomyces cerevisiae* from Old Mothers Display a Reduced Life Span. J. Cell Biol *127*, 1985–1993.

Kobayashi, T. (2003). The replication fork barrier site forms a unique structure with Fob1p and inhibits the replication fork. Mol. Cell. Biol. *23*, 9178–9188.

Kume, K., Cantwell, H., Neumann, F.R., Jones, A.W., Snijders, A.P., and Nurse, P. (2017). A systematic genomic screen implicates nucleocytoplasmic transport and membrane growth in nuclear size control. PLoS Genet. *13*, e1006767.

Lessard, F., Igelmann, S., Trahan, C., Huot, G., Saint-Germain, E., Mignacca, L., Del Toro, N., Lopes-Paciencia, S., Le Calvé, B., Montero, M., et al. (2018). Senescence-associated ribosome biogenesis defects contributes to cell cycle arrest through the Rb pathway. Nat. Cell Biol. *20*, 789–799.

Mansisidor, A., Molinar, T., Jr., Srivastava, P., Dartis, D.D., Pino Delgado, A., Blitzblau, H.G., Klein, H., and Hochwagen, A. (2018). Genomic copy-number loss is rescued by self-limiting production of DNA circles. Mol. Cell *72*, 583–593.e4.

McMurray, M.A., and Gottschling, D.E. (2003). An age-induced switch to a hyper-recombinational state. Science *301*, 1908–1911.

Miyazaki, T., and Kobayashi, T. (2011). Visualization of the dynamic behavior of ribosomal RNA gene repeats in living yeast cells. Genes Cells *16*, 491–502.

Mortimer, R.K., and Johnston, J.R. (1959). Life span of individual yeast cells. Nature *183*, 1751–1752.

Neumann, F.R., and Nurse, P. (2007). Nuclear size control in fission yeast. J. Cell Biol. *179*, 593–600.

Neurohr, G.E., Terry, R.L., Sandikci, A., Zou, K., Li, H., and Amon, A. (2018). Deregulation of the G1/S-phase transition is the proximal cause of mortality in old yeast mother cells. Genes Dev. *32*, 1075–1084.

Neurohr, G.E., Terry, R.L., Lengefeld, J., Bonney, M., Brittingham, G.P., Moretto, F., Miettinen, T.P., Vaites, L.P., Soares, L.M., Paulo, J.A., et al. (2019). Excessive Cell Growth Causes Cytoplasm Dilution And Contributes to Senescence. Cell *176*, 1083–1097.e18.

Nishimura, K., Kumazawa, T., Kuroda, T., Katagiri, N., Tsuchiya, M., Goto, N., Furumai, R., Murayama, A., Yanagisawa, J., and Kimura, K. (2015). Perturbation of ribosome biogenesis drives cells into senescence through 5S RNP-mediated p53 activation. Cell Rep. *10*, 1310–1323.

Rempel, I.L., Crane, M.M., Thaller, D.J., Mishra, A., Jansen, D.P., Janssens, G., Popken, P., Akşit, A., Kaeberlein, M., van der Giessen, E., Steen, A., Onck, P.R., Lusk, C.P., and Veenhoff, L.M. (2019). Age-dependent deterioration of nuclear pore assembly in mitotic cells decreases transport dynamics. eLIFE. https://doi.org/10.7554/eLife.48186.

Ren, X., Hu, B., Song, M., Ding, Z., Dang, Y., Liu, Z., Zhang, W., Ji, Q., Ren, R., Ding, J., et al. (2019). Maintenance of Nucleolar Homeostasis by CBX4 Alleviates Senescence and Osteoarthritis. Cell Rep. *26*, 3643–3656.e7.

Saka, K., Ide, S., Ganley, A.R., and Kobayashi, T. (2013). Cellular senescence in yeast is regulated by rDNA noncoding transcription. Curr. Biol. *23*, 1794–1798.

Saveanu, C., Bienvenu, D., Namane, A., Gleizes, P.E., Gas, N., Jacquier, A., and Fromont-Racine, M. (2001). Nog2p, a putative GTPase associated with pre-60S subunits and required for late 60S maturation steps. EMBO J. *20*, 6475–6484.

Shcheprova, Z., Baldi, S., Frei, S.B., Gonnet, G., and Barral, Y. (2008). A mechanism for asymmetric segregation of age during yeast budding. Nature *454*, 728–734.

Sinclair, D.A., and Guarente, L. (1997). Extrachromosomal rDNA circles–a cause of aging in yeast. Cell *91*, 1033–1042.

Sinclair, D.A., Mills, K., and Guarente, L. (1997). Accelerated aging and nucleolar fragmentation in yeast *sgs1* mutants. Science *277*, 1313–1316.

Smeal, T., Claus, J., Kennedy, B., Cole, F., and Guarente, L. (1996). Loss of transcriptional silencing causes sterility in old mother cells of S. cerevisiae. Cell *84*, 633–642.

Takeuchi, Y., Horiuchi, T., and Kobayashi, T. (2003). Transcription-dependent recombination and the role of fork collision in yeast rDNA. Genes Dev. *17*, 1497–1506.

Tiku, V., Jain, C., Raz, Y., Nakamura, S., Heestand, B., Liu, W., Späth, M., Suchiman, H.E.D., Müller, R.U., Slagboom, P.E., et al. (2017). Small nucleoli are a cellular hallmark of longevity. Nat. Commun. *8*, 16083.

Veatch, J.R., McMurray, M.A., Nelson, Z.W., and Gottschling, D.E. (2009). Mitochondrial dysfunction leads to nuclear genome instability via an iron-sulfur cluster defect. Cell *137*, 1247–1258.

## STAR★METHODS

### KEY RESOURCES TABLE

| REAGENT or RESOURCE | SOURCE | IDENTIFIER |
|---|---|---|
| Chemicals, Peptides, and Recombinant Proteins | | |
| Sylgard® 184 silicone polymer | World Precision Instruments LTD | Cat#SYLG184 |
| Paraformaldehyde (PFA)16% ultra-pure methanol free | Electron Microscopy Sciences | Cat#50-980-487 |
| Sorbitol | Sigma | Cat#S1876 |
| Zymolyase 20T | Euromedex | Cat#UZ1000 |
| Phenylmethylsulfonyl fluoride (PMSF) | Fischer Scientific | Cat#10485015 |
| Vanadyl Ribonucleoside Complex (Vanadium) | Sigma | Cat#R3380 |
| Mercaptoethanol-2 98% (βME) | Sigma | Cat#M3148 |
| Formamide | Sigma | Cat#F-5786 |
| Bovine Serum Albumin (BSA) | MP Biomedicals | Cat#841033 |
| tRNA from *E. coli* | Roche Diagnostics | Cat# 10109541001 |
| Triton X-100 | Sigma | Cat#T8787 |
| Experimental Models: Organisms/Strains | | |
| *S. cerevisiae*: strain TMY8: MATa; ade2::pAFS144-wtGFP(ADE2); rDNA::pTM-lacO50 (URA3) amplified ~150 copies NET1-mCherry-spHIS5, leu2-3,112 trp1-1 can1-100 ura3-1 ade2-1 his3-11,1 | (Miyazaki and Kobayashi, 2011) | N/A |
| *S. cerevisiae:* strain TMY8-BY4B: MATa; ade2::pAFS144-wtGFP(ADE2); rDNA::pTM-lacO50 (URA3) amplified ~150 copies NET1-mCherry-spHIS5; leu2Δ0; LYS2; MET15; TRP1 | This study | N/A |
| *S. cerevisiae*: strain RPA190-GFP: from S288C, MATa; RPA190-GFP-HIS3MX; ADE2; leu2Δ0; LYS2; met15Δ0; ura3Δ0; TRP1 | Thermo Fischer scientific | Yeast GFP Clone Collection |
| *S. cerevisiae*: strain SSF1-GFP: from S288C, MATa; SSF1-GFP-HIS3MX; ADE2; leu2Δ0; LYS2; met15Δ0; ura3Δ0; TRP1 | Thermo Fischer scientific | Yeast GFP Clone Collection |
| *S. cerevisiae*: strain NOG2-GFP: from S288C, MATa; NOG2-GFP-HIS3MX; ADE2; leu2Δ0; LYS2; met15Δ0; ura3Δ0; TRP1 | Thermo Fischer scientific | Yeast GFP Clone Collection |
| *S. cerevisiae*: strain RPL13A-GFP: from S288C, MATa; RPL13A-GFP-HIS3MX; ADE2; leu2Δ0; LYS2; met15Δ0; ura3Δ0; TRP1 | Thermo Fischer scientific | Yeast GFP Clone Collection |
| *S. cerevisiae*: strain YCG01: from S288C, MATa; ADE2; his3Δ1; leu2Δ0; lys2Δ0; met15Δ0; ura3Δ0; TRP1; HTB2-sfGFP-KANMX | (Garmendia-Torres et al., 2018) | N/A |
| *S. cerevisiae*: strain SJ164: from S288C, MATα; ADE2; his3Δ1; leu2Δ0; lys2Δ0; MET15; ura3Δ0; TRP1SP25::SP25-Act1p-NLS-sfGFP-STOP-Adh1t-NatMX | This study | N/A |
| *S. cerevisiae*: strain YAP160-1: from S288C, MATa; ADE2; his3Δ1; leu2Δ0; LYS2; met15Δ0; ura3Δ0; TRP1; SP25::SP25-Act1p-sfGFP-STOP-Adh1t-NatMX | This study | N/A |
| *S. cerevisiae*: strain SRP1-GFP: from S288C, MATa; SRP1-GFP-HIS3MX; ADE2; leu2Δ0; LYS2; met15Δ0; ura3Δ0; TRP1 | Thermo Fischer scientific | Yeast GFP Clone Collection |
| *S. cerevisiae*: strain BY4742: from S288C, MATα; ADE2; his3Δ1; leu2Δ0; lys2Δ0; MET15; ura3Δ0; TRP1 | Euroscarf | Cat#Y10000 |
| *S. cerevisiae*: strain YCG02: from S288C, MATα; ADE2; his3Δ1; leu2Δ0; lys2Δ0; MET15; ura3Δ0; TRP1; HTB2-sfGFP-KANMX | (Garmendia-Torres et al., 2018) | N/A |
| *S. cerevisiae*: strain fob1Δ: from S288C, MATα; ADE2; his3Δ1; leu2Δ0; lys2Δ0; MET15; ura3Δ0; TRP1; fob1::kanMX4 | Euroscarf | Cat#Y14044 |
| *S. cerevisiae*: strain sir2Δ: from S288C, MATα; ADE2; his3Δ1; leu2Δ0; lys2Δ0; MET15; ura3Δ0; TRP1; sir2::kanMX4 | Euroscarf | Cat#Y13738 |

(*Continued on next page*)

*Continued*

| REAGENT or RESOURCE | SOURCE | IDENTIFIER |
|---|---|---|
| *S. cerevisiae*: strain SM627: same as TMY8-BY4B except MATα; lys2Δ0; fob1::KANMX | This study | N/A |
| *S. cerevisiae*: strain SM546: from S288C, MATα; RPA190-GFP-HIS3MX; fob1::KANMX; ADE2; leu2Δ0; LYS2; MET15; ura3Δ0; TRP1 | This study | N/A |
| *S. cerevisiae*: strain SM345: from S288C, MATα; HTB2-sfGFP-KANMX; fob1::KANMX; ADE2; leu2Δ0; lys2Δ0; met15Δ0; ura3Δ0; TRP1 | This study | N/A |
| *S. cerevisiae*: strain SM550: from S288C, MATa; ADE2; his3Δ1; leu2Δ0; lys2Δ0; MET15; ura3Δ0; TRP1; sir2::kanMX4; fob1::kanMX4 | This study | N/A |
| *S. cerevisiae*: strain SM613: same as TMY8-BY4B except sir2::KANMX | This study | N/A |
| Oligonucleotides | | |
| ITS1 FISH probe: GCACAGAAATCTCTCACCGTTTGGAATAGCAAG AAAGAAACTTACAAGC + 5′ Cy3 | This study | N/A |
| Recombinant DNA | | |
| pDM402: SIR2 in pRS315 backbone (CEN LEU2 AmpR) | From Moazed laboratory. Provided by Paola Fabrizio | N/A |
| Software and Algorithms | | |
| NIS Element AR | Nikon | N/A |
| MATLAB R2016a | MathWorks | N/A |
| Phylocell | (Goulev et al., 2017) | https://www.github.com/gcharvin |
| Autotrack | (Goulev et al., 2017) | https://www.github.com/gcharvin |

## LEAD CONTACT AND MATERIALS AVAILABILITY

Further information and requests for resources and reagents should be directed to and will be fulfilled by the Lead Contact, Gilles Charvin (charvin@igbmc.fr).

## EXPERIMENTAL MODEL AND SUBJECT DETAILS

*Saccharomyces cerevisiae* is the experimental model used in this study. All strains are congenic to S288C, except TMY8 and TMY8-BY4B, and listed in the Key Resources Table.

## METHOD DETAILS

### Yeast strains, plasmids, and media

TMY8-BY4B was obtained from backcrossing four times with BY4742/BY4741 the strain TMY8 provided by Prof. Takehiko Kobayashi. All GFP-labeled strains were from the Yeast GFP Clone Collection provided by Michael Knop (Huh et al., 2003). *fob1Δ* and *sir2Δ* strains were purchased from Euroscarf, crossed with strains containing the relevant GFP markers, and genotyped by PCR. As *sir2Δ* strain is sterile and in order to cross it, this strain was transformed with pDM402, a non-integrative plasmid containing SIR2 gene. After crossing, strains of interest were counter-selected for pDM402 plasmid loss by checking their inability to grow in synthetic dextrose (SD) medium without leucine. The Htb2-sfGFP (Garmendia-Torres et al., 2018), Act1pr-sfGFP (sfGFP), and Act1pr-NLS-sfGFP (NLS-sfGFP) strains were generated using DNA editing and yeast genetics classical techniques.

Prior to loading into microfluidic chips, freshly thawed cells were grown overnight in synthetic complete medium with 2% dextrose and then diluted in the morning to allow several divisions in exponential growth.

### Microfluidics

The microfluidic master mold was made using standard soft-lithography techniques in the FEMTO-ST nanotechnology platform of the French Renatech network (Besançon, France). Prototypic molds were replicated in epoxy to ensure long-term preservation. The micro-channels were cast by curing PDMS (Sylgard 184, 10:1 mixing ratio) and then covalently bound to a 24 × 50 mm coverslip using plasma surface activation (Diener, Germany). The assembled chip was then baked for 1 h at 60°C to consolidate bonding between the glass and PDMS and then perfused with media using Tygon tubing and a peristaltic pump (Ismatec, Switzerland) at a 10 μl/min flow rate. After 2 h of PDMS rehydration, yeast cells were loaded into the chip with a 1 mL syringe and a 23G needle.

### RNA FISH-on-a-CHIP

Time-lapse imaging was stopped after 65 h acquisition and the chip was perfused with 4% paraformaldehyde for 30 min at room temperature (RT) and then washed for 20 min with buffer B (1.2 M sorbitol, 0.1 M potassium phosphate, pH 7.5). The cell walls were digested by flowing a zymolyase mix (0.2mg/ml Zymolyase 20T, 0.2mM PMSF, 2mM Vanadium, 29mM βME) through the chip for 20 min at RT followed by a 20 min wash with buffer B. The chip was then rinsed with cold 70% ethanol for 5 min, with 2xSSC (saline-sodium citrate) for 15 min, and with 10% formamide in 2xSSC for 20 min. A hybridization mix containing 1 ng/μl FISH probe (in 2xSSC, 10% formamide, 10mM Vanadium, 0.5mg/ml BSA, 0.5mg/ml tRNA) was injected into the chip and the cells were incubated at 37°C for 3 h, protected from light. The cells were then rinsed with warm (37°C) 10% formamide in 2xSSC for 30 min, 1% Triton X-100 in 2xSSC for 20 min, and 1xSSC for 30 min. The cells were then imaged on a Nikon Ti-Eclipse with an mCherry filter to acquire the FISH probe signal (50% LED power, 300 ms exposure time, binning 2 × 2) and a GFP filter to acquire the Rpa190-GFP (20% led power, 100 ms exposure time, binning 2 × 2) as well as in phase contrast. The FISH probe (with a 5′ Cy3 dye) targets the ITS1 region between the A2 cleavage site and the 18S coding region.

### Time-lapse microscopy

Cells were imaged using an inverted Nikon Ti-E microscope. Fluorescence illumination was achieved using LED light (Lumencor) and emitted light was collected using a 60 × N.A. 1.4 objective and a CMOS camera Hamamatsu Orca Flash 4.0. An automated stage was used to follow up to 60 different fields of view in parallel over the course of the experiment. Images were acquired every 10 or 15 min for a total duration of 140 h (full lifespan experiments) or 65 h (RNA FISH experiments) using NIS software. Focus was maintained using the Nikon Perfect Focus System. A constant temperature of 30°C was maintained on the chip using a custom sample holder with thermoelectric modules, an objective heater with heating resistors, and a PID controller (5C7-195, Oven Industries).

### Image analysis

After acquisition, NIS raw data were analyzed using the custom MATLAB software phylocell and autotrack, available on https://www.github.com/gcharvin. Cell contours and fluorescent markers were segmented using a modified watershed algorithm and tracking was achieved with the Hungarian method, as previously described (Goulev et al., 2017). Cell area was measured from the segmentation of the phase contrast images (Figure 2F). Nuclear and nucleolar areas were measured from the segmentation of Htb2-sfGFP signal (Figures 4C, 4D, and 5I) and Net1-mCherry signal (Figure 5C) respectively.

### Data analysis

As birth alignment blurs the dynamics of aging (Figure S1), we aligned single-cell trajectories from the onset of cell cycle slowdown (or SEP). To determine the SEP, we calculated the frequency of division for each individual cellular lifespan and we used piecewise linear model to determine the time beyond which the frequency of division rapidly declines (see Figure S2). Therefore, cells that have passed the SEP are not strictly in a senescent state, yet, they have started to undergo an irreversible physiological decline leading to cell death. The determination of the SEP is then systematically used as a reference of time to assess the average dynamics of specific markers throughout the manuscript, unless specified otherwise (e.g., Figures S3E-S3H).

A least-square minimization technique was used to fit GFP-LacI data to an exponential model (Figure 1E), excluding data points associated with late senescence (i.e., > SEP + 3 divisions), during which the GFP-LacI saturates.

### Computational simulations of replicative lifespan

We designed a stochastic numerical model to describe the replicative lifespan of individual cells in which ERCs are excised and allowed to amplify, as previously described (Gillespie et al., 2004). For convenience, instead of discrete probability distributions, we used an analogy to a biochemical system with continuous time based on the following assumptions: 1) an ERC is randomly excised from the genome with a rate $k_e$ per generation; Multiple ERC excisions are allowed during the course of the simulation, yet this does not much influence the exponential dynamics of ERCs, which is set by the first excision event; 2) Following a mechanism of self-replication, ERCs accumulate exponentially within the mother cell, with a doubling-time $\tau$ (per generation), the value of which is measured experimentally. Hence, in the case of $\tau > 1$ generations, this rule assumes that the efficiency of replication may be lower than 100% or, alternatively, that some ERCs may be inherited by daughter cells; 3) Once the number of ERCs within a mother cell overcomes a threshold $ERC^{thr}$, the cell division cycle starts to be impaired (SEP) and cell death occurs randomly with a rate $k_s$ per generation, as observed experimentally (Figure 6).

We used the Gillespie algorithm (Gillespie, 1977) to generate 200 single cell trajectories according to this set of rules, in which the number of ERCs copies was simulated over time. Then, we extracted the numerical distribution of timings associated with the three main events that compose the lifespan of cells, i.e., the excision of the first ERC, the onset of entry into senescence (SEP), and cell death (Figure 7).

To account for the fact that a large fraction of *fob1Δ* cells die without any observable ERC accumulation, we used a Gompertz law to model an ERC-independent path to senescence, with a hazard rate λ defined as:

$$\lambda(age) = \lambda_0 e^{\mu\ age}$$

where $\lambda_0$ is the initial mortality rate and $\mu$ is the rate of increase of the mortality rate with age. Therefore, the cells died either following excision and accumulation of ERC or from an alternative cause that did not lead to a cell cycle slow down (SEP), and the fraction of cells with SEP was calculated within the population of simulated cells.

## QUANTIFICATION AND STATISTICAL ANALYSIS

All experiments have been replicated at least twice. Data are presented in Results and Figures as the mean ± SEM (curves) or median (boxplots). Boxplots show the median, the notch (95% confidence interval of the median), the 25$^{th}$ quantile, the 75$^{th}$ quantile, extreme data points and outliers. ****$p < 0.0001$, t test. Group means were compared using Two-sample t test. A P value of $< 0.05$ was considered significant.

## DATA AND CODE AVAILABILITY

The custom MATLAB software phylocell and autotrack, used to analyze imaging data are available on https://www.github.com/gcharvin.